A New numerical method 'for surface hydrodynamics

Article *in* Journal of Geophysical Research Atmospheres · October 1987

DOI: 10.1029/JC092iC11p11803

5 authors, including:

Bruce J West
United States Army
532 PUBLICATIONS **12,414** CITATIONS

JOURNAL OF GEOPHYSICAL RESEARCH, VOL. 92, NO. C11, PAGES 11,803–11,824, OCTOBER 15, 1987

A New Numerical Method for Surface Hydrodynamics

BRUCE J. WEST,[1] KEITH A. BRUECKNER,[2] AND RALPH S. JANDA

Division of Applied Nonlinear Problems, La Jolla Institute, La Jolla, California

D. MICHAEL MILDER AND ROBERT L. MILTON

Areté Associates, Sherman Oaks, California

We present a new numerical method for studying the evolution of free and bound waves on the nonlinear ocean surface. The technique, based on a representation due to Watson and West (1975), uses a slope expansion of the velocity potential at the free surface and not an expansion about a reference surface. The numerical scheme is applied to a number of wave and wave train configurations including longwave–shortwave interactions and the three–dimensional instability of waves with finite slope. The results are consistent with those obtained in other studies. One strength of the technique is that it can be applied to a variety of wave train and spectral configurations without modifying the code.

1. INTRODUCTION

The wind generation of waves on the ocean surface and their subsequent evolution has been described for over 2 decades in terms of a weakly interacting field of nonlinear waves whose equations of motion are determined by a Hamiltonian [*Phillips*, 1966; *Zakharov*, 1968] for an incompressible, inviscid, irrotational liquid. To describe the processes of wave generation, evolution, and the subsequent development of wave instabilities, it has been found convenient to express the observables at the ocean surface in series expansions of the eigenfunctions of the linearized system. The expansion coefficients in such series are constant in the linearized systems but are variable in the nonlinear system. Because the linear water wave field is harmonic, the eigenfunctions are simple sines and cosines, and the series expansion are just Fourier series. The expansion coefficients are interpreted as the amplitudes of independent waves in a linear wave field. Correspondingly, the nonlinear surface is referred to as a nonlinear wave field, and the nonlinearities are interpreted as couplings or scatterings of the once linear waves [*Hasselmann*, 1962, 1963*a*,*b*]. The Hamiltonian for this system is a series in which the nonlinear terms appear as products of the mode amplitudes [e.g., *West*, 1981]. These nonlinear interactions induce variations in both the amplitudes and the phases of the linear waves in the equations of motion. For a weakly nonlinear system such as gravity waves away from the region of wave breaking, this induced variation is much slower than the harmonic variation of the linearized system [*Phillips*, 1960; *Benney*, 1962; *Longuet–Higgins*, 1962].

The gravity wave field on the sea surface is a conservative Hamiltonian system so that Hamilton's equations of motion provide a deterministic description of its evolution [*Hasselmann*, 1968; *Broer*, 1974; *Watson and West*, 1975; *Miles*, 1977; *Milder*, 1977; *West*, 1981]. If we assume that this field is well represented by N degrees of freedom, where N may be large but finite, the system can be represented by N coupled, deterministic, nonlinear rate equations for the mode amplitudes. *Moser* [1973] gives a general mathematical discussion of the separation of the interactions in such Hamiltonian systems into resonant and nonresonant groups. The nonresonant interactions provide for a stable evolution in the phase space of the system, whereas the resonant interactions lead to instabilities. In a qualitative way, a resonance is a matching between both space and time scales of the wave of interest and the scale of the nonlinear interactions among the other waves. The existence of such resonance in water wave fields was explicitly pointed out by *Phillips* [1960]. He showed that just as for resonance in a linear system, the resonant nonlinear interactions among gravity waves produces an initial secular growth of new waves. *Benney* [1962] extended these arguments to show how the nonlinear interactions also lead to an eventual quenching of this apparent instability. *Chirkov* [1979], in his discussion of the general properties of nonlinear systems, points out that the oscillations induced by such nonlinear resonances are always bounded, as distinct from linear resonances which are unbounded in general. The dependence of the frequency on the wave amplitude, i.e., the nonlinear dispersion relation, is the cause of the nonlinear resonant motion being bounded. The weak nonlinearities in the system therefore act to stabilize the system motion and inhibit explosive instabilities.

The concept of resonant interaction has formed the basis for many analytic–numeric calculations of the properties of wind–generated water waves [*Hasselmann*, 1962, 1963*a*,*b*; *Zakharov*, 1968; *Yuen and Lake*, 1982; *Peregrine*, 1983; *Bryant*, 1984]. The evolution of capillary and gravity–capillary waves has been described by mode rate

[1] Also at Institute of Nonlinear Science, University of California, San Diego, La Jolla.

[2] Also at Department of Physics, University of California, San Diego, La Jolla.

Paper number 7C0303.
0148-0227/87/007C–00303$05.00

equations with quadratic nonlinearities, i.e., three–wave interactions, whereas gravity waves are described by mode rate equations with cubic nonlinearities, i.e., four–wave interactions. The nonresonant interactions had been thought to be unimportant in describing the evolution of the wave field; however, *Watson and West* [1975] using perturbation theory and *West* [1981] using a canonical transformation of variables, demonstrated that the nonresonant terms contribute substantially to the strength of the resonant interactions among the surface waves and are therefore not negligible. In this paper we include the effects of both linear and nonlinear interactions.

In this age of the computer, an efficient computational technique can be at least as useful in probing the physical content of a system of dynamic equation as the analysis of a number of exactly solvable special cases. In this paper we present such a numerical technique for solving the nonlinear partial differential equations describing the evolution of free waves on the ocean surface. Numerical codes using this technique are then applied to a number of wave and wave train configurations that are fairly well understood to establish the integrity of the technique.

The technique is the culmination of work by the various authors spanning several years. As far as we know the first proposal for a method of this kind applied to the nonlinear ocean surface appeared in an unpublished memorandum of 1974 by one of us (BJW) and his colleagues J. Alex Thomson and Kenneth Watson. The method was independently proposed and implemented in one surface dimension by another of us (DMM) in 1977. The computations possible at the time were limited by computer size and speed to fairly modest scales and idealized one–dimensional problems, but they were able to demonstrate strikingly realistic nonlinear behavior. Some of the calculations to be shown have been done previously using special–purpose codes, but the approach presented here is among the first that has been able to do them all without modification of the code.

Herein we do not model the ocean surface as a weakly interacting wave field in the sense developed by *Zakharov* [1968]; i.e., we do not truncate the mode rate equations at third order in the mode amplitudes nor do we restrict the interactions to those at or near resonance. Rather, the formal expansion about the free surface of Bernoulli's equation and the kinetic boundary condition are retained to arbitrary order using a formalism developed by *Watson and West* [1975]. The numerical integration of these latter equations is done by taking products of field quantities in configuration space, e.g., the surface displacement, velocity potential, and gradients of these terms; fast Fourier Transforming (FFT) the configuration equations and time incrementing the transformed equations to obtain the components of the appropriate field variables, then transforming (FFT) back to configuration space to again evaluate the nonlinear products and start the process again. This numerical procedure described in section 2 does not distinguish between resonant and nonresonant interactions, so that it includes effects explicitly neglected, or approximated by most calculations involving the use of nonlinear mode rate equations. In particular, herein we do not make a multiple time scale expansion to construct the mode rate equations [*Yuen and Lake*, 1982].

In section 3 we present a number of calculations using the new technique. Some of these, such as soliton propagation and scattering, reproduce well–known results. However, certain stability properties of envelope solitons are determined that could not be observed previously because of computational limitations. We also examine the persistence of modulational patterns on the ocean surface such as Kelvin wakes as well as three–dimensional wave instabilities.

Of most significance to physical oceanography has been the use of these nonlinear equations in constructing transport expressions for the action or energy density in a wind–generated gravity wave field [*Hasselmann*, 1962, 1963*a*,*b*, 1968; *Longuet–Higgins and Cokelet*, 1976]. By assuming the statistics of the surface waves to be Gaussian, the resonant waves have been shown to lead to an integro differential transport equation that is cubic in the action spectral density $[N(\mathbf{k},t)]$ [*Hasselmann*, 1962, 1963*a*,*b*; *West*, 1981]. It is well known that the equilibrium spectrum determined by this equation is nonphysical; i.e., $N(\mathbf{k},\infty) \approx (\alpha+\boldsymbol{\beta}\cdot\mathbf{k}+\gamma\omega_k)^{-1}$ where $\alpha, \boldsymbol{\beta}$ and γ are constants, $\mathbf{k}$ is the wave vector, and ω_k is the wave frequency, so a more exact treatment of the evolution of the action density is desirable. In particular, one that leads to an equilibrium spectrum that is physically realizable.

Hasselmann [1962, 1963*a*,*b*] assumed a priori that the nonlinear wave field on the ocean surface is spatially homogeneous. In more usual situations the transport equations will contain both homogeneous and nonhomogeneous terms. The former dominate the description of the long–term, large–scale oceanographic forecasting of the wave spectrum even though these terms are weaker and slower than the nonhomogeneous terms [*Watson and West*, 1975]. The latter terms dominate the smaller–scale phenomena that would be of interest in the interpretation of returns from remote sensors such as radar. The description of the modulational characteristics of the ocean surface would be an essential part of such an interpretation, and the nonhomogeneous aspect of the transport equation must be properly taken into account [*Watson, West, and Cohen*, 1976; *Yuen and Lake*, 1982].

The homogeneous transport equation of Hasselmann has been evaluated only in a relatively few situations because of the excessive computational time required to evaluate the five–dimensional integral in the nonlinear energy transfer term. Various approximations of the integral expression based on narrow–peaked spectrum approximations have been made [*Longuet–Higgins*, 1976; *Fox*, 1976; *Dungey and Hui*, 1979; *Herterich and Hasselmann*, 1980]. *Hasselmann and Hasselmann* [1985] have pointed out that although these approximations faithfully yield some important features of the full integral expression, "they are not sufficiently accurate to serve as an acceptable parameterization in wave models." These latter authors discuss a computational technique which exploits the explicit symmetries of the integrand of the homogeneous transport equation and introduce a stretched variable to enhance resolution in important regions of wave vector space [*Hasselmann and Hasselmann*, 1981].

In section 3.5 some aspects of energy transfer have been considered for the interaction of waves of very different wavelength and height, showing the rapid alteration of the shorter wavelength spectrum. This rapid energy transfer also shows that a perturbation treatment has limited validity. This conclusion is relevant to the more general ques-

tion of convergence of the Watson–West and Hasselmann methods when waves of very different amplitude and wavelength are present.

Section 3.6 illustrates the ability of this method to reproduce sharp–crested waves, both steady and random. The example of parasitic capillaries arising at the crest of a gravity–wave train is another illustration of the simultaneous convergence of the free surface slope expansion at widely differing height and wavelength scales.

2. WATSON-WEST METHODOLOGY

2.1. *Basic Equations*

The motion of the free surface of an incompressible, inviscid liquid $h(\mathbf{x}, t)$ is determined by the Bernoulli equation

$$\frac{\partial \phi}{\partial t} + \frac{1}{2}\mathbf{v}^2 + gh = 0 \tag{1}$$

with the fluid velocity $\mathbf{v}(\mathbf{x}, t)$ given by the gradient of the velocity potential $\phi(\mathbf{x}, t)$,

$$\mathbf{v} = \nabla\phi \tag{2}$$

and the vertical motion of the free surface by

$$\frac{dh}{dt} = \frac{\partial h}{\partial t} + \mathbf{v}\cdot\nabla h = \frac{\partial \phi}{\partial z} \equiv W \tag{3}$$

In the interior of the incompressible fluid,

$$\nabla\cdot\mathbf{v} = 0$$

so that

$$\nabla^2\phi = 0 \tag{4}$$

These equations can be easily converted to equations at the free surface, where

$$\phi_s(\mathbf{x}, t) = \phi[\mathbf{x}, h(\mathbf{x}, t), t] \tag{5}$$

with the result (dropping the subscript s on ϕ_s)

$$\begin{aligned} \frac{\partial \phi}{\partial t} &= -gh - \frac{1}{2}[\nabla\phi]^2 + \frac{1}{2}W^2[1 + (\nabla h)^2] \\ \frac{\partial h}{\partial t} &= -\nabla\phi\cdot\nabla h + W[1 + (\nabla h)^2] \end{aligned} \tag{6}$$

These equations form a canonical pair,

$$\frac{\partial \phi}{\partial t} = -\frac{\delta H}{\delta h} \qquad \frac{\partial h}{\partial t} = \frac{\delta H}{\delta \phi} \tag{7}$$

derivable from a single Hamiltonian function

$$H(h, \phi) = \frac{1}{2}\int\left[\phi\frac{\partial h}{\partial t} + gh^2\right] d\mathbf{x} \tag{8}$$

in which $\partial h/\partial t$ is understood to stand for the linear functional of ϕ in (6) as developed below [*Broer* (1974); *Miles* (1977)]. The nonlinear terms in both field equations arise from the nonlinear dependence of the kinetic energy terms on surface slope. The approximations to be used are based on truncations of the Hamiltonian at various nonlinear orders. The essence of this method is that the dynamics or *forces* are approximated, but the *solutions* are unconstrained. For example the advective term $\nabla\phi\cdot\nabla h$ in the height equation (6) originates in the first nonlinear term of the Hamiltonian, but it can, along with its counterpart $(\nabla\phi)^2/2$ in the potential equation, generate sharp–crested waves. The solution of (6) depends on obtaining an equation for W in terms of h and ϕ.

The procedure proposed by *Watson and West* [1975] starts from the formal relationship

$$\phi(\mathbf{x}, h) = \sum_n \frac{h^n}{n!}\frac{\partial^n}{\partial z^n}\Phi(\mathbf{x}) \tag{9}$$

with

$$\Phi(\mathbf{x}) = \phi(\mathbf{x}, z) \qquad z = 0$$

and h measured from a reference height $z = 0$, but this reference height is arbitrary; we could choose it as h_0. In (9) the derivative of ϕ can be expressed in terms of the formal operator

$$\frac{\partial}{\partial z} \equiv \kappa \tag{10}$$

which multiplies any one– or two–dimensional Fourier coefficient of ϕ by the magnitude of $\mathbf{k}$. From $\phi(\mathbf{x}, z)$, the vertical velocity is given by

$$\begin{aligned} W &= \frac{\partial}{\partial z}\phi(\mathbf{x}, z) \qquad \text{at } z = h \\ &= \sum_n \frac{h^n \kappa^{n+1}}{n!}\Phi(\mathbf{x}) \end{aligned} \tag{11}$$

Given $\phi(\mathbf{x}, h)$, the reference function $\Phi(\mathbf{x})$ can be obtained by formally inverting (9), and finally W can be obtained from the infinite series (11).

The field equations (6) must be truncated at consistent nonlinear order if they are to represent a conservative Hamiltonian system. The order is counted as the power of h or its gradient occurring in the terms associated with W; at order n,

$$\begin{aligned} W[1 + (\nabla h)^2] &\to W_n + W_{n-2}(\nabla h)^2 \\ \frac{1}{2}W^2[1 + (\nabla h)^2] &\to \frac{1}{2}(W^2)_n + \frac{1}{2}(W^2)_{n-2}(\nabla h)^2 \end{aligned} \tag{12}$$

with

$$(W^2)_n = \sum_{m=0}^{n} W_m W_{n-m} \tag{13}$$

The solution of these equations can be obtained by formal expansions of W and ϕ as

$$\begin{aligned} W &= \sum_{n=0}^{\infty} W_n \\ \phi &= \sum_{n=0}^{\infty} \Phi_n \end{aligned} \tag{14}$$

with the terms in W and ϕ ordered according to their dependence on h. From the expansion in (9), we find

$$\begin{aligned} \phi &= \Phi_0 \\ 0 &= h\kappa\Phi_0 + \Phi_1 \\ 0 &= \frac{1}{2}h^2\kappa^2\Phi_0 + h\kappa\Phi_1 + \Phi_2 \\ 0 &= \sum_{m=0}^{n}\frac{(h)^{n-m}(\kappa)^{n-m}}{(n-m)!}\Phi_m \end{aligned} \tag{15}$$

giving the inversion

$$\Phi_0 = \phi$$
$$\Phi_1 = -h\,\kappa\Phi_0$$
$$\Phi_2 = -h\,\kappa\Phi_1 - \frac{1}{2}h^2\kappa^2\Phi_0$$
$$\Phi_3 = -h\,\kappa\Phi_2 - \frac{1}{2}h^2\kappa^2\Phi_1 - \frac{1}{3!}h^3\kappa^3\Phi_0$$
$$\Phi_n = -\sum_{m=1}^{n}\frac{(h)^m\,\kappa^m}{m!}\,\Phi_{n-m} \tag{16}$$

From (11), we then find

$$W_0 = \kappa\Phi_0$$
$$W_1 = \kappa\Phi_1 + h\,\kappa^2\Phi_0$$
$$W_2 = \kappa\Phi_2 + h\,\kappa\Phi_1 + \frac{1}{2}h^2\kappa^3\Phi_3$$
$$W_3 = \kappa\Phi_3 + h\,\kappa^2\Phi_2 + \frac{1}{2}h^2\kappa^3\Phi_1 + \frac{1}{3!}h^3\kappa^4\Phi_0$$
$$W_n = \sum_{m=0}^{n}\frac{(h)^m\,(\kappa)^m}{m!}\,\Phi_{n-m} \tag{17}$$

Computationally, (16) is solved in sequence giving the Φ of each order in terms of the Φ of lower order and h. From the Φ the W_n are then obtained in sequence from (17).

The series for W has been obtained by a formal expansion about a reference surface $z=0$. The method therefore is not obviously valid if the reference surface is shifted or if very different wavelengths and wave heights are present. The series can, however, easily be seen to be a slope expansion so that the wave height does not directly enter. If h is shifted by a constant h_0 only differences in h enter the series. This is also apparent from the definitions of the series in (9) and (11). If we shift h by a constant amount h_0, we can rewrite Eqs. (9) and (11) as

$$\Phi_s = \sum_n \frac{(h+h_0)^n\,\kappa^n}{n!}\,\Phi$$
$$\equiv \sum_n \frac{h^n\kappa^n}{n!}\,e^{\kappa h_0}\Phi \tag{18}$$
$$W = \sum_n \frac{(h+h_0)^n\,\kappa^{n+1}}{n!}\,\Phi$$
$$\equiv \sum_n \frac{h^n}{n!}\,\kappa^{n+1}\,e^{\kappa h_0}\Phi \tag{19}$$

This arrangement is possible since h_0 commutes with κ. The same expression $e^{\kappa h_0}\Phi$ appears in Eqs. (18) and (19) so that the choice of h_0 does not affect the relationship between W and Φ_s and only shifts the reference function Φ. The calculation has been carried out with a spectrum covering a wavelength ratio of 1024 (linear mesh of 4196 points) with all portions of the spectrum behaving stably, and only slow energy transfer occurring. Further tests of stability and convergence are described in section 2.4.

2.2. *Computational Procedure*

The principal computational problem is the evaluation of (16) and (17). From the W_n values so obtained, the time evolution equations (6) are easily advanced.

The evaluation of the κ operations in (16) and (17) is most simply carried out by the FFT algorithm. The operations of even power in κ can in principle be carried out by using the identity

$$\kappa^2 F(\mathbf{x}) = -\left(\nabla_x^2+\nabla_y^2\right)F(\mathbf{x})$$
$$= \int d^2k\,\left(k_x^2+k_y^2\right)\tilde{F}(\mathbf{k})\,e^{i\mathbf{k}\cdot\mathbf{x}} \tag{20}$$

where $\tilde{F}(\mathbf{k})$ is the Fourier transform of the arbitrary function $F(\mathbf{x})$ and using a low-order finite difference formula to evaluate the surface Laplacian. This procedure can, however, affect the accuracy and convergence of the calculations, since the FFT evaluation of κ^2 and the finite difference evaluation of $-\nabla^2$ are significantly different, particularly in high Fourier components. We have found that this error can lead to instability for high Fourier components. The method we have developed therefore evaluates all κ^n operations by the method of FFT.

The time evolution equations for ϕ and h contain nonlinear terms, the order depending on the approximation used for W. If the calculation is formally of order n and the Fourier transforms of h and ϕ contain maximum Fourier components $k_m = 2\pi m/L$, the nonlinear products will contain Fourier components $n\,k_m$. These will produce Fourier space aliasing if

$$n\,m > N/2 \tag{21}$$

N is the number of mesh points in the x or y direction, assumed to be equal. The aliasing will give spurious components to a distance $(N-n\,m)$ below $N/2$. These will enter into h and ϕ unless $(N-n\,m)$ does not enter into the band $k<k_m$, giving the nonaliasing condition

$$N - n\,m \geq m \tag{22}$$

or

$$m \leq \frac{N}{n+1} \tag{23}$$

This limit severely restricts the Fourier space which can be kept and therefore limits the effective resolution of the calculations. The minimum wavelength in terms of the mesh size Δ is

$$\lambda_{\min} = \frac{2\pi}{k_{\max}} = \frac{L}{m} = \frac{L}{N}(n+1)$$
$$= \Delta(n+1) \tag{24}$$

Thus for $n=1$, $\lambda_{\min}=2\Delta$. For a calculation of third order, $\lambda_{\min}=4\Delta$. For the same spatial resolution, the mesh size in a third-order calculation therefore must be ½ the mesh of a first-order calculation. If the calculation is in the fifth order, $\lambda_{\min}$ is 6Δ, requiring a mesh of ⅓ for the same resolution as the first order.

2.3. *Time Integration*

The surface displacement and velocity potential can be expanded in the discrete Fourier series

$$h(\mathbf{x},t) = \sum_{\mathbf{k}} e^{i\mathbf{k}\cdot\mathbf{x}}h_{\mathbf{k}}(t) \tag{25}$$
$$\phi_s(\mathbf{x},t) = \sum_{\mathbf{k}} e^{i\mathbf{k}\cdot\mathbf{x}}\phi_{\mathbf{k}}(t) \tag{26}$$

The coupled equations for the Fourier amplitudes $h_{\mathbf{k}}$ and $\phi_{\mathbf{k}}$ obtained from (6) are of the form

$$\begin{aligned} \frac{\partial h_{\mathbf{k}}}{\partial t} &= \kappa \phi_{\mathbf{k}} + A_{\mathbf{k}} \\ \frac{\partial \phi_{\mathbf{k}}}{\partial t} &= -g h_{\mathbf{k}} + B_{\mathbf{k}} \end{aligned} \tag{27}$$

with $A_{\mathbf{k}}$ and $B_{\mathbf{k}}$ containing the nonlinear terms [e.g., *West*, 1981]. These equations are unstable for any time step if they are advanced explicitly. They are also unstable if advected by a combination of implicit and explicit differences if the Courant conditions

$$c_{x_{\max}} \Delta t < \Delta x \qquad c_{y_{\max}} \Delta t < \Delta y \tag{28}$$

are violated, with $c_{x_{\max}}$ and $c_{y_{\max}}$ the maximum phase speeds of a wave in the x and y direction, respectively.

The integration scheme must accommodate the time variation of the driving terms A_k, B_k, which can depend markedly on the situation. For example in a progressive narrow-band wave train the dominant driving forces would constitute an overtone series of the dominant wave such that for each spatial overtone k' the $A_{k'}, B_{k'}$ would be narrow–band temporal processes centered about the overtone frequency $\omega' = ck'$, c being the fundamental phase speed. Under such circumstances the time behavior can be modeled with slowly varying parameters so that large time steps and high efficiency can be attained. A scheme of this kind has been developed and tested on the code in use at the La Jolla Institute, and is described immediately below. More chaotic situations in which waves of many wavelengths propagate in many directions generate broadband temporal variation in the A_k, B_k, and one might expect this particular method to experience more trouble. One can always fall back on the less efficient small time steps bounded by the Courant condition above. We have found that very broadband, random surfaces can be modeled with acceptable efficiency by a simple explicit time step, and have installed their variant in the code running at Areté Associates. This method, though formally unstable, has an exponential growth rate that becomes numerically trivial for time steps more dense than a few per cycle.

For the narrow–band case, assume that the time dependence at an near t_n can be approximated by

$$\begin{aligned} A_{\mathbf{k}}(t) &= A_{\mathbf{k}}(t_n) \exp i\, \omega_0 (t - t_n) \\ B_{\mathbf{k}}(t) &= B_{\mathbf{k}}(t_n) \exp i\, \omega_1 (t - t_n) \end{aligned} \tag{29}$$

Equations (27) and (29) then can be combined to give

$$\begin{aligned} \frac{\partial^2 h_{\mathbf{k}}}{\partial t^2} &= -g \kappa h_{\mathbf{k}} + A_{\mathbf{k}}(t_n)\, i\, \omega_0 \exp\left[i\, \omega_0 (t - t_n) \right] \\ &\quad + \kappa B_{\mathbf{k}}(t_n) \exp\left[i\, \omega_1 (t - t_n) \right] \end{aligned} \tag{30}$$

This equation has a solution

$$\begin{aligned} h_{\mathbf{k}} = {} & C_1 e^{i\omega(t - t_n)} + C_2 e^{-i\omega(t - t_n)} \\ & + C_3 e^{i\omega_0 (t - t_n)} + C_4 e^{i\omega_1 (t - t_n)} \end{aligned} \tag{31}$$

with the linear wave dispersion relation for deep–water gravity waves

$$\omega^2 = g\, |\mathbf{k}| \tag{32}$$

Using (27) – (31) we find

$$\begin{aligned} & h_{\mathbf{k}}(t_n) = C_1 + C_2 + C_3 + C_4 \\ & i\, \omega (C_1 - C_2) + i\, \omega_0 C_3 + i\, \omega_1 C_4 = \kappa \phi_{\mathbf{k}}(t_n) + A_{\mathbf{k}}(t_n) \\ & (\omega^2 - \omega_0^2) C_3 = i\, \omega_0 A_{\mathbf{k}}(t_n) \\ & (\omega^2 - \omega_1^2) C_4 = \kappa B_{\mathbf{k}}(t_n) \end{aligned} \tag{33}$$

From which we obtain C_1, C_2, C_3, C_4 as functions of $A_{\mathbf{k}}(t_n)$, $B_{\mathbf{k}}(t_n)$, ω_0, and ω_1, for each value of $\mathbf{k}$.

To utilize this method, we have adopted a two–step procedure. The time dependence of $A_{\mathbf{k}}$ and $B_{\mathbf{k}}$ is first obtained from a backward difference, i.e.,

$$\begin{aligned} A_{\mathbf{k}}(t_{n-1}) &= A_{\mathbf{k}}(t_n) \exp\left[i\, \omega_0 (t_{n-1} - t_n) \right] \\ B_{\mathbf{k}}(t_{n-1}) &= B_{\mathbf{k}}(t_n) \exp\left[i\, \omega_1 (t_{n-1} - t_n) \right] \end{aligned} \tag{34}$$

giving a first estimate of the complex constants ω_0 and ω_1. This allows $h_{\mathbf{k}}(t_{n+1})$ and $\phi_{\mathbf{k}}(t_{n+1})$ to be obtained, and from these provisional values, $\hat{A}_{\mathbf{k}}(t_{n+1})$ and $\hat{B}_{\mathbf{k}}(t_{n+1})$ computed directly from $h_{\mathbf{k}}(t_{n+1})$ and $\phi_{\mathbf{k}}(t_{n+1})$. The provisional values are used in a second pass to obtain improved values of ω_0 and ω_1 i.e.,

$$\begin{aligned} \hat{A}_{\mathbf{k}}(t_{n+1}) &= A_{\mathbf{k}}(t_n) \exp\left[i\, \omega_0 (t_{n+1} - t_n) \right] \\ \hat{B}_{\mathbf{k}}(t_{n+1}) &= B_{\mathbf{k}}(t_n) \exp\left[i\, \omega_1 (t_{n+1} - t_n) \right] \end{aligned} \tag{35}$$

This method has been found to be stable and accurate for time steps several times the Courant condition of (28).

2.4. *Stability and Convergence*

The computational procedure outlined in this section can be applied to a variety of problems of general interest and of more special interest to oceanographers. The order of the calculations is practically limited to fifth or sixth order. Experience has shown that the series in powers of wave height or slope converges slowly as the breaking limit is approached, requiring other approximations for very steep waves.

In practice, a test for stability and accuracy is routinely applied. This results from computations of the total energy.

$$E = \int dx\, dy \left[\phi \frac{\partial h}{\partial t} + g h^2 \right] \tag{36}$$

and the components of the total momentum components

$$p_i = \int dx\, dy\, \frac{\partial \phi}{\partial x_i}\, h \tag{37}$$

These are very accurately (1 part in 10^4) conserved when very steep waves do not develop. It bears emphasizing that the energy is conserved order by order in the mode amplitudes, i.e., at third and fifth order separately in the approximate calculations. If, however, local wave breaking occurs, a marked drift in the energy occurs and the calculation will terminate because of numerical divergence. The energy can also drift if the time step has been chosen to be too large a multiple of the Courant condition.

The tests utilizing (36) and (37) show when the calculation is inaccurate because of either the time step used or waves which are steepening and approaching the breaking point. Reducing the time step may stabilize the calculation, but more probably, particularly with many component spectra with random phases assigned, a local interference

TABLE 1. Fourier Moduli for Case 1 ($h_0=0.05$, $k=2\pi$)

n	Vortex	WW 3	WW 5
1	2.44×10^{-2}	2.44×10^{-2}	2.44×10^{-2}
2	3.65×10^{-3}	3.67×10^{-3}	3.64×10^{-3}
3	1.17×10^{-3}	1.17×10^{-3}	1.13×10^{-3}
4	4.24×10^{-4}	4.90×10^{-4}	4.02×10^{-4}

The wave number is $2\pi n$. The time is $t=0.5125$. The column labeled "vortex" contains the lowest four Fourier amplitudes obtained from the three-dimensional vortex code. The other columns are the third and fifth order calculations using the Watson–West method.

pattern has occurred which causes local wave breaking. The calculation has not yet been adapted to include dissipative effects to simulate the passage through a wave-breaking region.

In the development of the formalism and numerical structure of the method of this paper, a number of tests were made in one surface dimension, comparing the Watson–West expansion with the vortex sheet method summarized in the Appendix. To obtain high accuracy of the vortex sheet calculations, several careful checks of convergence methods of evaluating the Green's function and its singularities and of obtaining slope derivatives were employed. These are generally similar to the methods outlined in the references cited in the appendix. Further details will be given in a separate paper now in preparation.

The results of the example calculations are summarized in Tables 1, 2, and 3. These examples are

Case 1: Single wave

$$k = 2\pi$$
$$h_0 = 0.05$$
$$h(t=0) = h_0 \sin kx$$
$$\phi(t=0) = \left(-h_0/\sqrt{k}\right)\cos kx \tag{38}$$

Case 2: Single wave

$$k = 2\pi$$
$$h_0 = 0.075$$
$$h(t=0) = h_0 \sin kx$$
$$\phi(t=0) = \left(-h_0/\sqrt{k}\right)\cos kx \tag{39}$$

Case 3: Composite wave

$$k_1 = 2\pi$$
$$k_2 = 16\pi$$
$$h_1 = 0.025$$
$$h_2 = 0.025/8$$
$$h(t=0) = h_1 \sin(k_1 x) + h_2 \sin(k_2 x)$$
$$\phi(t=0) = \left(-h_1/\sqrt{k_1}\right)\cos k_1 x - \left(h_2/\sqrt{k_2}\right)\cos k_2 x \tag{40}$$

The Fourier moduli at selected times for several of the amplitudes are given in the tables. It should be noted that the single waves have slopes of 0.3142 and 0.4712. The first wave steepens and fluctuates in form but does not break; the second breaks at $t \cong 0.60$. The agreement between the vortex and the Watson–West calculations (particularly fifth order in the Fourier mode amplitude) is quite good, showing no appreciable systematic error. The agreement is well maintained for the two-wave mixture (Figure 1c and Table 3) with a height ratio of 8 between the waves. More extensive calculations have been made in one dimension with wavelength ratios of 1024 and amplitude ratios as high as 10^6 (Phillips spectrum) with good stability and convergence for all of the Fourier components.

TABLE 2. Fourier Moduli for Case 2 ($h_0=0.075$, $k=2\pi$)

	$t=0.3125$			$t=0.5125$	
n	Vortex	WW 3	WW 5	Vortex	WW 5
1	3.71×10^{-2}	3.70×10^{-2}	3.71×10^{-2}	3.57×10^{-2}	3.58×10^{-2}
2	4.03×10^{-3}	4.08×10^{-3}	3.99×10^{-3}	7.38×10^{-3}	7.20×10^{-3}
3	1.68×10^{-3}	1.71×10^{-3}	1.56×10^{-3}	3.27×10^{-3}	3.30×10^{-3}
4	7.60×10^{-4}	9.43×10^{-4}	6.86×10^{-4}	1.63×10^{-3}	1.46×10^{-3}
5	3.76×10^{-4}	5.04×10^{-4}	3.19×10^{-4}	8.73×10^{-4}	7.84×10^{-4}
6	1.98×10^{-4}	3.10×10^{-4}	1.66×10^{-4}	4.96×10^{-4}	4.00×10^{-4}
7	1.07×10^{-4}	2.09×10^{-4}	0.84×10^{-4}	2.75×10^{-4}	2.44×10^{-4}

The wave number is $2\pi n$. The times are 0.3125 and 0.5125. For the latter case the third-order Watson–West diverged so it was necessary to go to fifth order.

To study phenomena of oceanographic interest, a maximum wavelength of the order of 100 m, with the phase velocity corresponding to a 12.6-m/s wind speed, could be included in the area analyzed with a minimum wavelength of the order of 1 m, requiring for a third-order calculation a mesh of 25 cm. The corresponding number of mesh points is 400×400 for a square mesh and area. The Courant conditions for this mesh and maximum phase velocity is 0.02 s. The time stepping procedures described in section 2.2 allow the time step to be increased to about 0.2 s. The period of the longest wave is 1.26 s; the calculation should follow many wave periods and therefore run for the order of 1 min or for about 300 time steps.

TABLE 3. Fourier Moduli for Case 3 ($h_1=0.025$, $k_1=2\pi$; $h_2=0.025/8$, $k_2=16\pi$) at $t=0.5125$

n	Vortex	WW 3	WW 5
1	1.241×10^{-2}	1.242×10^{-2}	1.242×10^{-2}
2	1.000×10^{-4}	0.983×10^{-4}	0.977×10^{-4}
3	1.63×10^{-4}	1.64×10^{-4}	1.60×10^{-4}
4	3.24×10^{-5}	3.76×10^{-5}	2.59×10^{-5}
5	1.30×10^{-6}	1.26×10^{-6}	1.47×10^{-6}
6	1.41×10^{-4}	1.63×10^{-4}	1.68×10^{-4}
7	7.12×10^{-4}	8.48×10^{-4}	8.29×10^{-4}
8	10.70×10^{-4}	9.35×10^{-4}	9.62×10^{-4}
9	8.23×10^{-4}	7.75×10^{-4}	7.82×10^{-4}
10	4.05×10^{-4}	3.71×10^{-4}	3.78×10^{-4}
11	1.78×10^{-4}	1.74×10^{-4}	1.60×10^{-4}
12	0.80×10^{-4}	0.85×10^{-4}	0.64×10^{-4}
13	0.38×10^{-4}	0.79×10^{-4}	0.53×10^{-4}

At $t=0$, the $n=1$ and $n=8$ amplitudes were 2.5×10^{-2} and 3.125×10^{-3}. The large change in the amplitudes, particularly around $n=8$, is the result of strong interactions with the $n=1$ wave.

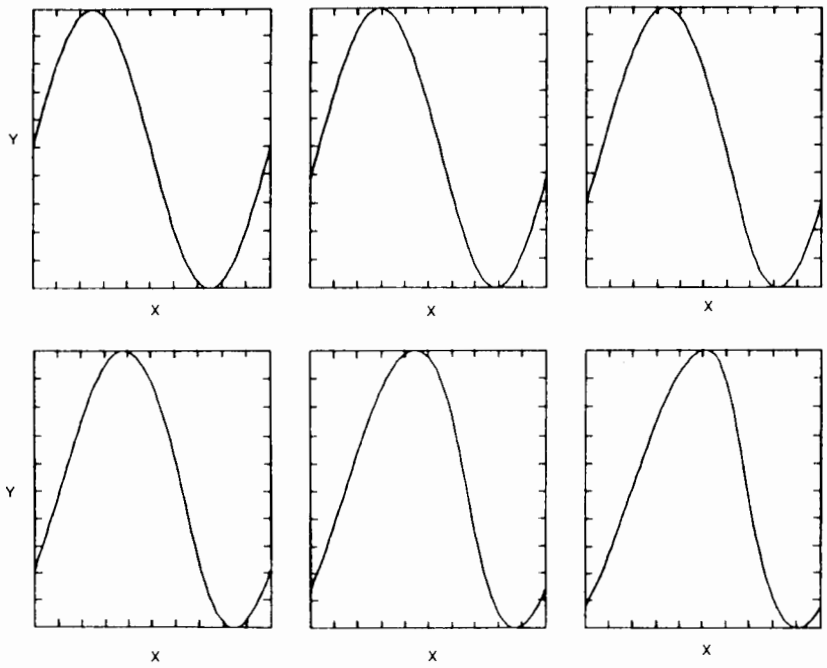

Fig. 1*a*. Wave amplitude for case 1 ($h_0 = 0.05$, $k = 2\pi$) as a function of time (z stat).

The computing time is primarily determined by the FFT time. On the code in use at the La Jolla Institute the time on the Cray X-MP for the third-order calculations in a 256 × 256 spatial grid for a single FFT pair is 0.094 s. The time for a complete double-pass calculation (predictor, corrector) per time step is 2.73 s. The code at Areté, using a faster than standard FFT completes an entire third order time step on a 512 × 512 grid in 0.50 seconds and on a 256 × 256 grid in 0.13 seconds. At a recommended twenty steps per cycle for the simple second-order predictor this amounts to 2.5 seconds/cycle for the shortest wave present.

3. APPLICATIONS

3.1. *Soliton Stability*

The weak interaction equations have been used to study a variety of surface wave instabilities, in particular, the nonlinear Schrödinger equation, derivable from the mode rate equations [*Zakharov*, 1968; *Cohen et al.* 1976], has been used to model the evolution of a weakly nonlinear wave train [see *Yuen and Lake*, 1982, and references therein]. The envelope soliton solution to this equation predicted by

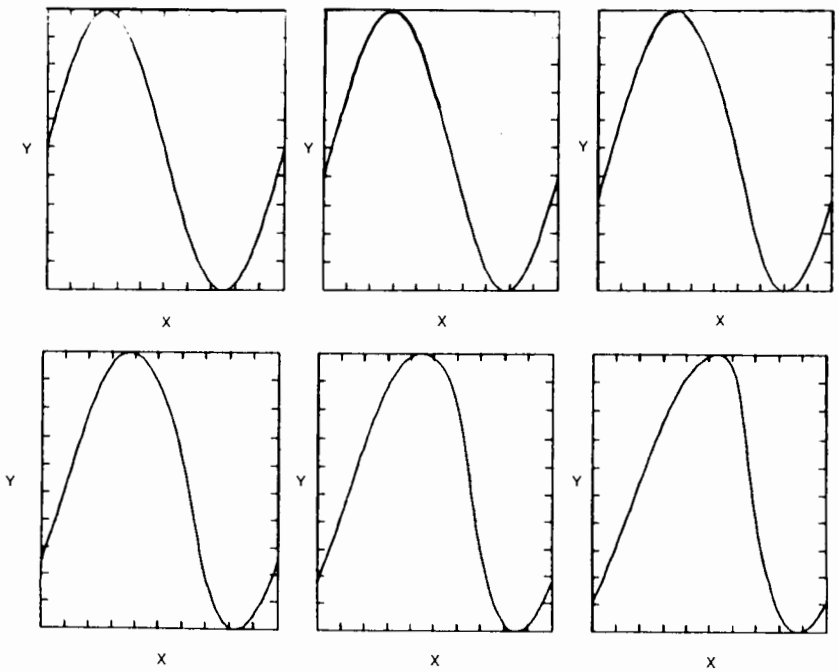

Fig. 1*b*. Wave amplitude for case 2 ($h_0 = 0.075$, $k = 2\pi$).

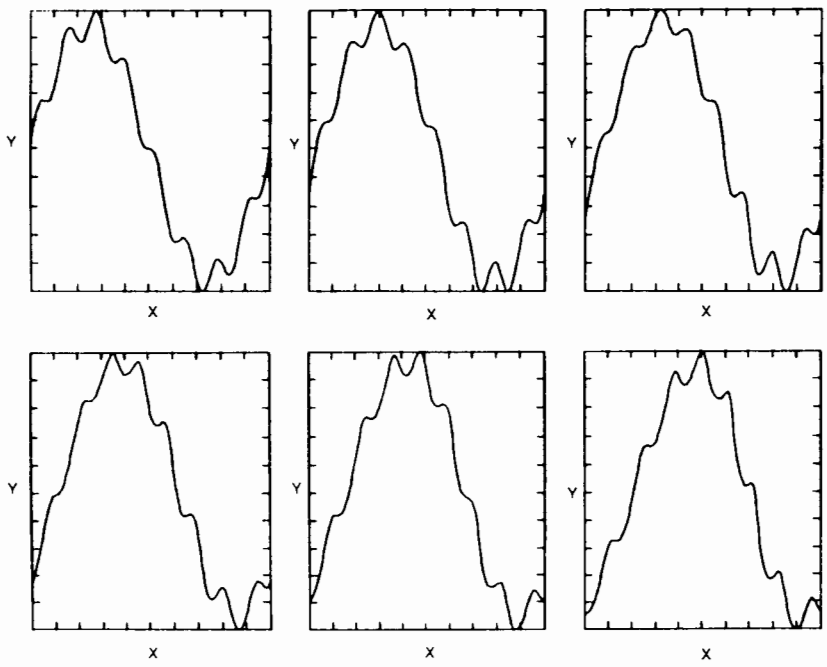

Fig. 1c. Wave amplitude for case 3.

Zakharov and Shabat [1972] was experimentally observed by *Lake et al.* [1977] and also calculated for water waves by *Cohen et al.* [1976] and *Bryant* [1979]. These coherent wave packets that balance the linear dispersion of the waves against the weak nonlinear interactions among the waves are distinct from the side band instabilities noted by *Benjamin and Feir* [1967] for nonlinear wave trains. The theoretical prediction of the Benjamin–Feir sideband instability is that of a breakup of a nonlinear wave with the energy eventually appearing in a number of small-amplitude randomized waves. With the identification of the soliton it was conjectured that the final state of an unstable Stokes wave would be one or more asymptotically stable solitons. *Lake et al.* [1977] found that instead of these two possible final states, what is observed is a periodic near-return of the wave train to the initial state of the system. The modulation induced by the instability periodically increases and decreases, so that even though energy is transferred to distant modes in the spectrum, once the magnitude of the modulation has reached some critical value, the initial state will reclaim nearly all of this distant energy with a definite reclamation frequency. This observed recurrence phenomena has been calculated using both the nonlinear Schrödinger equation and the four-wave resonant mode rate equations directly. It is found however that a soliton is unstable against transverse perturbation [*Cohen et al.*, 1976; *Saffman and Yuen*, 1978; *Martin et al.*, 1980] and therefore is probably not of general importance in oceanographic context. Further, the recurrence phenomenon, while interesting, does not persist in three dimensions.

Cohen et al. [1976] have shown that to a good approximation a one-dimensional solution to the nonlinear Schrödinger equation is given by the N-mode decomposition

$$Z(x,t) = \sum_n a_n(t) \exp i\, k_n x \tag{41}$$

where the initial mode amplitudes are given by

$$a_n(0) = a_N(0)\ \text{sech}\left[\frac{(N-n)\pi}{\sqrt{\delta m N}}\right] \tag{42}$$

The central wave number is $k_N = N\Delta k$, $\Delta k = 2\pi/L$ and the central amplitude $a_N(0)$ is determined by the condition

$$m = k_N \sum_n a_n(0) \tag{43}$$

From the complex amplitude $Z(x,t)$ the surface potential and wave height are given by

$$\phi = \kappa^{-1/2}\,\text{Re}\,Z \tag{44}$$

$$h = -\,\text{Im}\,Z \tag{45}$$

The soliton given by (41) is a solution to the full equations (6) only if the soliton is "thin," i.e., if the slope parameter m is small. As the slope increases, the soliton is expected to become unstable.

This problem has been solved on a 16×256 mesh using the technique described in section 2. Except where indicated, the calculations are carried out to third order in (13) with 4×64 Fourier components. The problem is scaled so that the horizontal scale is unity and $g = 1$. The maximum velocity is $c_{\max} = (2\pi)^{-1/2}$. The Courant condition is $\Delta t < \Delta x / c_{\max} = (2\pi)^{1/2}/256 = 0.0245$. The calculation runs stably and accurately for the time step used, which was 0.08. As a check on the calculation, the total energy and the two momentum components are computed with each time step. If a significant change in any of these conserved quantities occurs, a reduction in the time step is made until the conservation laws are well satisfied.

Figures 2 and 3 give temporal development of solitons with slopes $m = 0.16$ and $m = 0.256$. The thin soliton is quite stable but the "fat" soliton ($m = 0.256$) slowly radiates energy into wavelengths outside of the original spectrum.

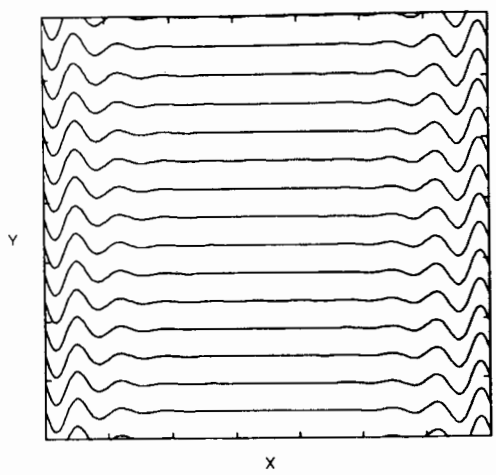

Fig. 2*a*

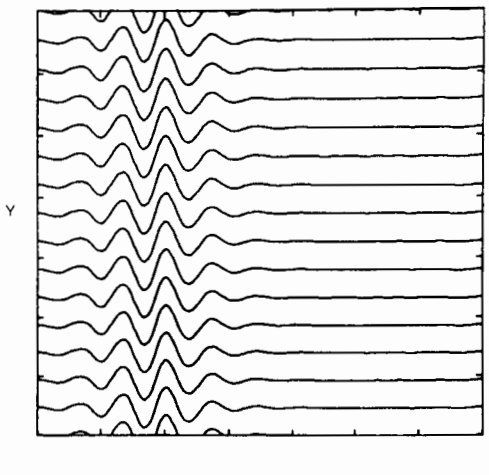

Fig. 2*b*

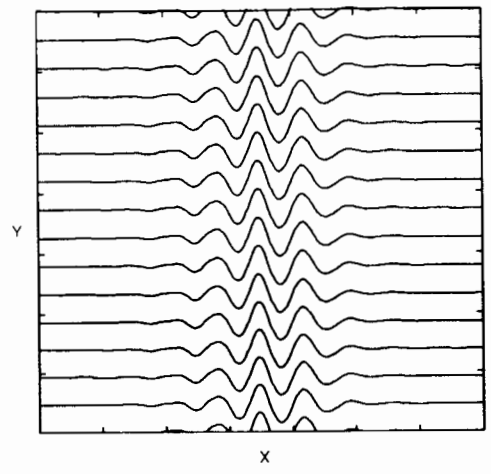

Fig. 2*c*

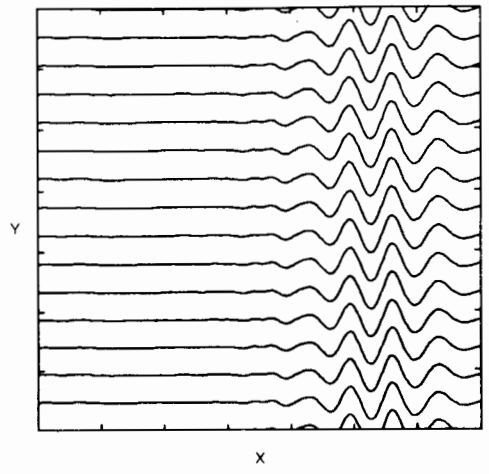

Fig. 2*d*

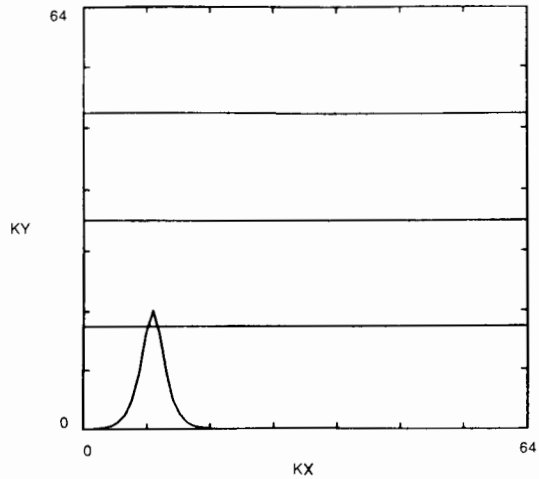

Fig. 2*e*

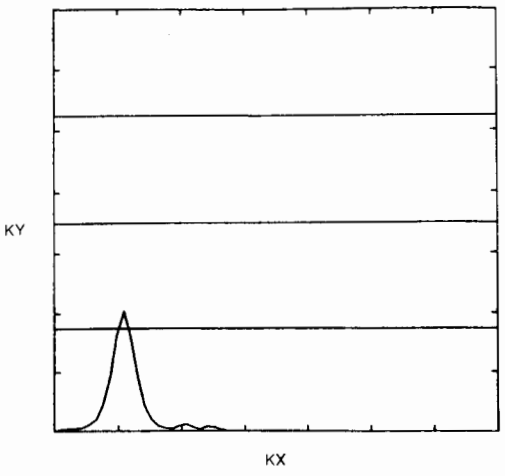

Fig. 2*f*

Fig. 2. Temporal development of the wave amplitude of a "thin" soliton with $m = 0.16$. Figures 2*a*, 2*b*, 2*c*, and 2*d* are at $t = 0, 4, 8, 12$. Figures 2*e* and 2*f* give the Fourier amplitudes at $t = 0, 12$.

The collision of two solitons has been computed for the same spatial mesh and time step. The development is given as Figure 4. Unlike the calculations based on the nonlinear Schrödinger equation [*Yuen and Lake*, 1982] or a few mode amplitudes [*Cohen et al.*, 1976], the solitons here are appreciably perturbed in the collision, and their structure is *not* preserved. The Fourier amplitudes also show marked alteration. This suggests that such coherent structures would not be sufficiently stable to influence the chaotic spectrum of wind wave spectra in the open ocean.

The interaction of a thin soliton with a large–amplitude long–wavelength field has also been determined. The soli-

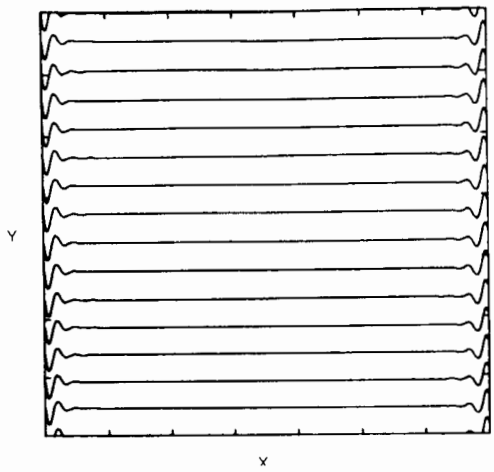

Fig. 3*a*

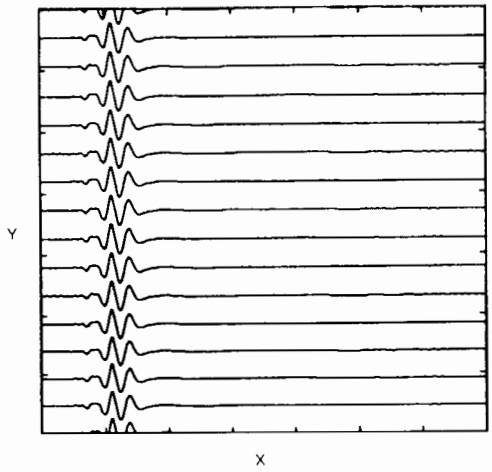

Fig. 3*b*

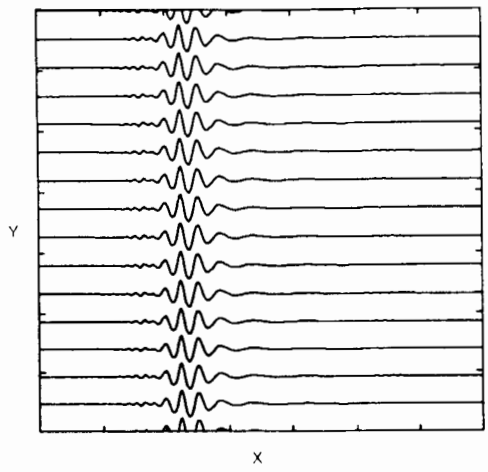

Fig. 3*c*

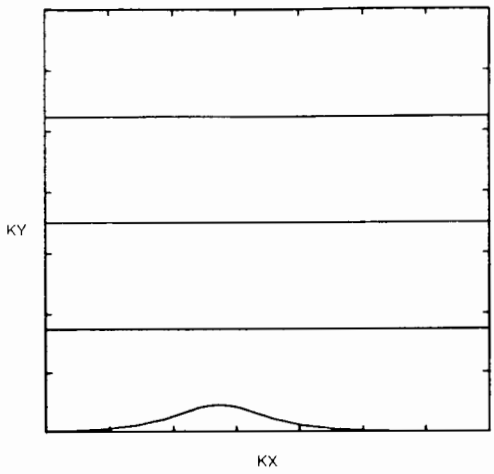

Fig. 3*d*

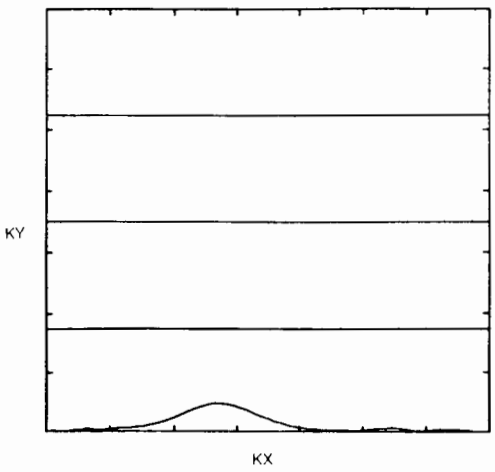

Fig. 3*e*

Fig. 3. Temporal development of a "fat" soliton with $m = 0.256$. Figures 3*a*, 3*b*, and 3*c* are at $t = 0, 4, 8.08$. Figures 3*d* and 3*e* give the Fourier amplitudes at $t = 0, 8$.

ton is the same as in Figure 2 with $m = 0.16$ and a central mode of $N = 10$. The long waves are modes 3 and 4, with amplitudes 5 times the central amplitude of the soliton. Figure 5 gives the propagation of the wave field with the Fourier amplitudes of modes 3 and 4 removed from the figure. The soliton is strongly perturbed by the long waves, failing to "ride over" their passage.

The one–dimensional solitons are also expected to be unstable against both a longitudinal side–band instability (the Benjamin–Feir mode) and a transverse perturbation.

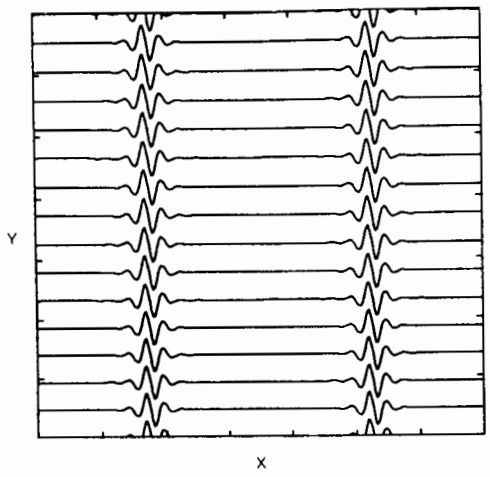

Fig. 4*a*

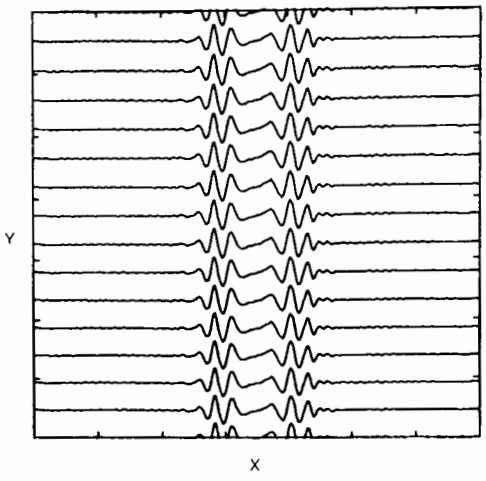

Fig. 4*b*

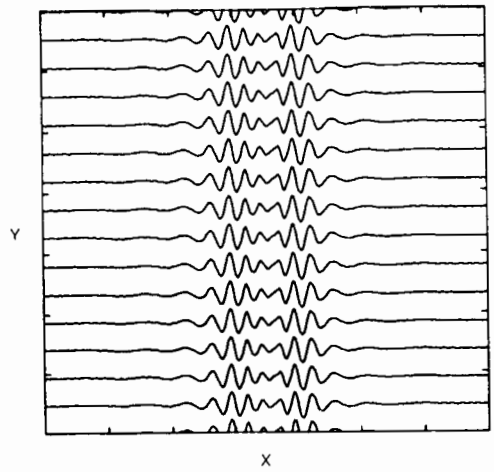

Fig. 4*c*

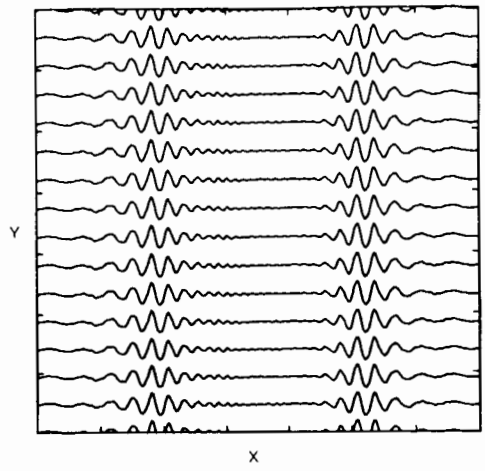

Fig. 4*d*

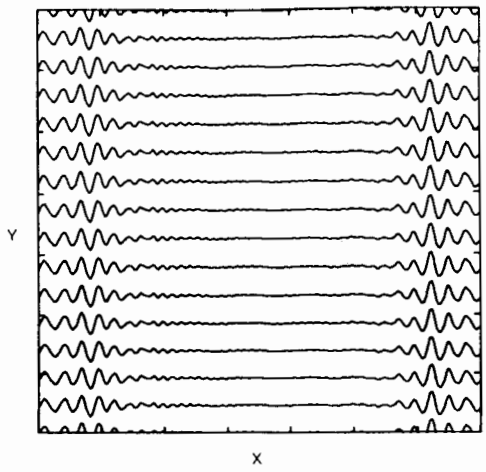

Fig. 4*e*

Fig. 4. Collision of two fat solitons. Figures 4*a*, 4*b*, 4*c*, 4*d*, and 4*e* are at $t = 0, 4, 8, 12, 16$.

The effect of a single–mode transverse perturbation has been computed for a 128 × 128 mesh in Figure 6. The transverse mode numbers 2, 4, 6 ($k_y = 4\pi, 8\pi, 12\pi$) were considered. The soliton has central mode number $N = 10$ and slope $m = 0.22$. The form of the perturbation is

$$\Delta Z = \Delta x \sum_n a_n e^{ik_n x} \cos(k_y y) \tag{46}$$

with $\Delta x = 0.1$. The mode number $n = 2$ grew by a factor of 2.2 in 36 time units, but the other modes showed no

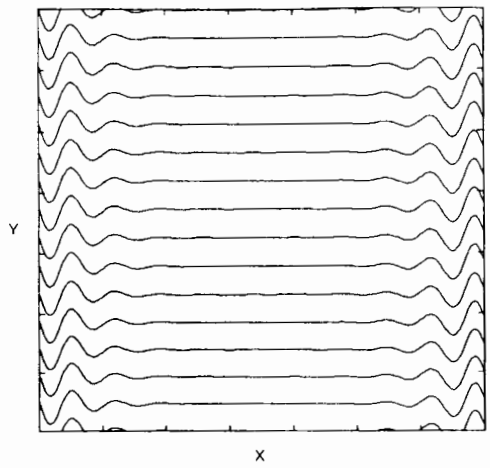

Fig. 5*a*

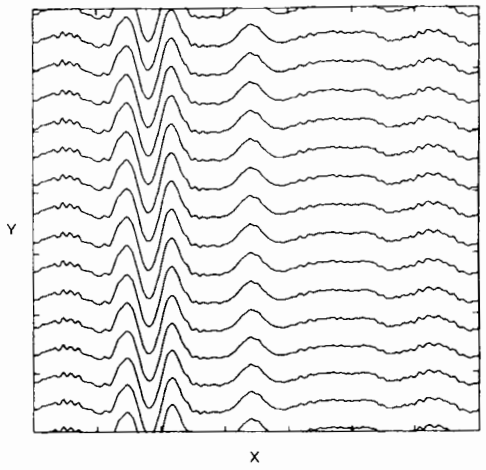

Fig. 5*b*

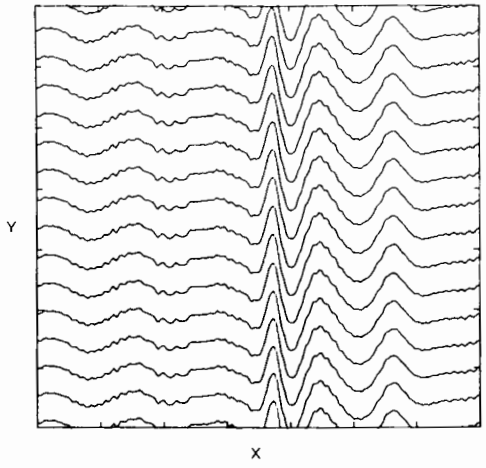

Fig. 5*c*

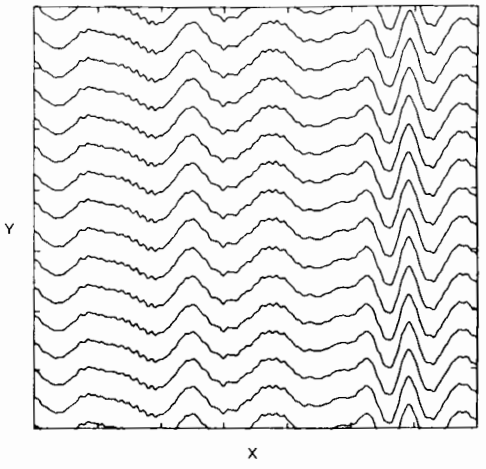

Fig. 5*d*

Fig. 5. Propagation of a thin soliton in the presence of large–amplitude, long–wavelength waves. The Fourier amplitudes of the long waves have been subtracted. Figures 5*a*, 5*b*, 5*c*, and 5*d* are at $t = 0, 4, 8, 12$.

significant growth. This fat soliton also radiated appreciable energy into longitudinal modes. The growth rate observed is 20% lower than that determined by *Cohen et al.* [1976] in the same parameter regime as the fat soliton.

A regular wave train will grow into an oblique wave group structure when it is modulated over a length scale that is large compared with its own wavelength because the modulation is unstable. *McLean et al.* [1981] and *McLean* [1982] showed that such oblique instabilities dominate parallel instabilities for wave slopes that are moderate to large. *Hui and Hamilton* [1979] calculated wave group solutions of the nonlinear Schrödinger (NLS) equation in two horizontal dimensions. If the wave field does not have a narrow central peak, however, the NLS equation fails as a model equation of the wave group structures. Secondary peaks can arise from resonant interactions among the waves, and *Bryant* [1984] showed that such resonances do not arise from oblique wave groups whose group–to–wave angle is less than $\tan^{-1}(0.5)$. For greater angles, resonances can be significant even to the extent that at some angles they dominate the oblique wave group structure. This situation can only be described by including the full nonlinear dynamics in the wave field.

3.2. *Three–Dimensional Instabilities*

The balance between the linear dispersion and the nonlinear interaction of water waves, so clearly evident in the use of the nonlinear Schrödinger equation, has been determined to be of secondary importance in describing the evolution of sea waves. The bifurcation of three–dimensional water waves, on the other hand, may well be an important energy transfer mechanism. As was pointed out by *Su and Green* [1984], most waves in developing seas are short crested, a characteristic property of three–dimensional instabilities and bifurcating waves. In the laboratory, both these phenomena have led to breaking waves, so that it is not unreasonable to expect that they will also produce breaking in the open ocean. Su and Green conjecture that these instabilities and bifurcation will create local "order" from the surrounding chaos of the ambient wave field.

Recently, observed gravity wave instabilities were shown to result from the bifurcation of three–dimensional waves arising from skew rather than colinear perturbations [*Su et al.*, 1982; *Su*, 1982]. Infinitely long perturbations were analyzed by *Peregrine and Thomas* [1979] using a modified version of Witham's theory and by *Saffman and*

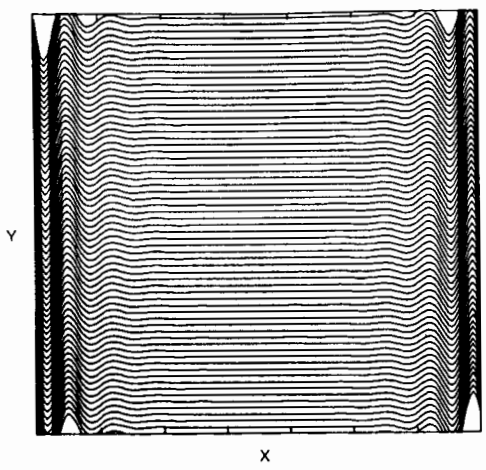

Fig. 6*a*

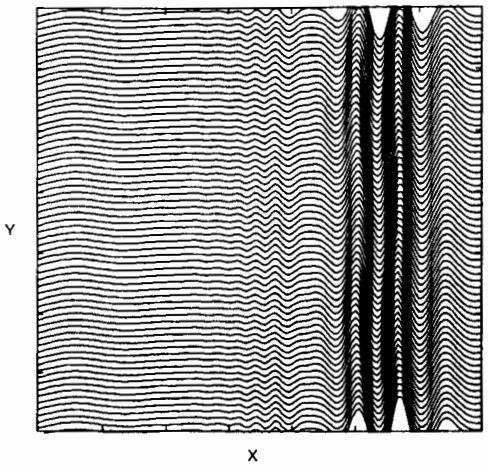

Fig. 6*b*

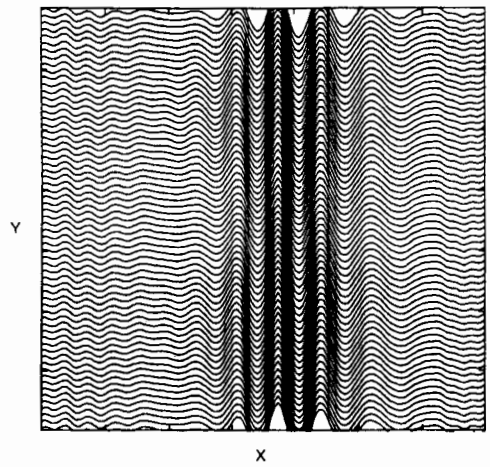

Fig. 6*c*

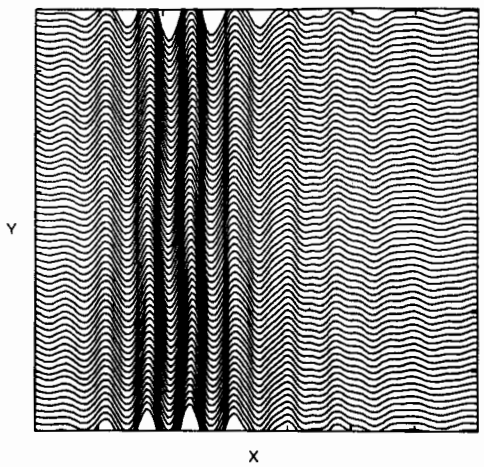

Fig. 6*d*

Fig. 6. Perturbation of a fat soliton with $m = 0.22$ by a transverse wave. Figures 6*a*, 6*b*, 6*c*, and 6*d* are at $t = 0, 12, 24, 36$. The Fourier amplitudes are given in Figures 6*e*, 6*f*, 6*g*, and 6*h* at $t = 0, 12, 24, 36$. The Fourier plots are labeled by mode number.

Yuen [1980] using the mode rate equations. These instabilities are studied herein using the new numerical technique.

In Figure 7*a* we depict a two–dimensional wave field for a long–crested wave ($k_0 a_0 = 0.30$) propagating in the positive x direction. The initial wave amplitude is

$$h = h_0 \cos k_0 x + h_1 \cos (k_1 x + k_2 y) + h_1 \cos (k_3 x + k_2 y)$$

with wave members

$$k_0 = 16\pi, \quad k_1 = 24\pi, \quad k_2 = 22\pi, \quad k_3 = -8\pi$$
$$h_0 k_0 = 0.3 \qquad h_1 = 0.2 h_0$$

The long–crested wave train is seen to undergo a rapid transition to a regular, symmetric, three–dimensional wave form. This is shown in Figures 7*b*–7*d* which correspond qualitatively to the photographs of symmetric bifurcations taken by *Su* [1982]. From Figures 8*a*–8*c* we visually estimate that the crestwise length of these crescent shaped bifurcated waves is between 0.8 and 0.85 of the wavelength of the unperturbed waves. There also appears to be a crestwise wave shift between two consecutive rows of crescent waves in agreement with the observed shift of one–half wavelength [*Su*, 1982] (compare Figure 8*c*). The diagnostics necessary for the code to provide a quantitative determination of the rate of growth of the instability for comparison with, e.g., the analytic calculation of *Saffman and Yuen* [1980], have not as yet been developed.

3.3. *Dissipation of Single Waves*

The persistence of a pattern of waves in the presence of a background wave field has been considered by many authors; most recently by Watson [1986]. He has investigated the persistence of a modulation pattern of the Kelvin wake of a surface ship in a surface gravity wave field. The mechanisms he investigated that promote wave pattern decay were viscous damping, air–sea interactions, and three–wave and four–wave interactions. The dominant mechanism turned out to be a function of wave number and wind speed. The longest wave perturbation decayed owing to the air–sea interaction, whereas the decay of those wavelengths that have a phase velocity much less that the average wind speed was dominated by the four–wave interactions. Herein we examine this problem by calculat-

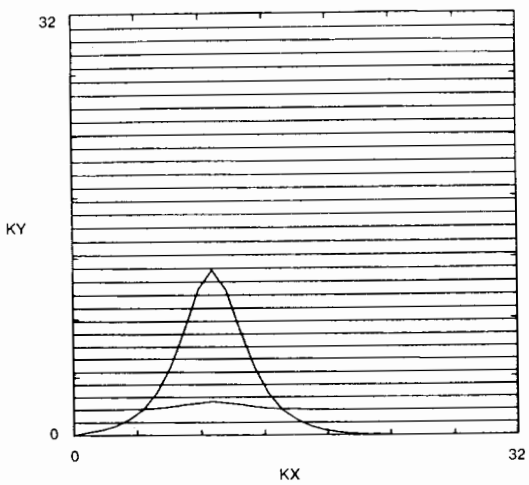

Fig. 6e

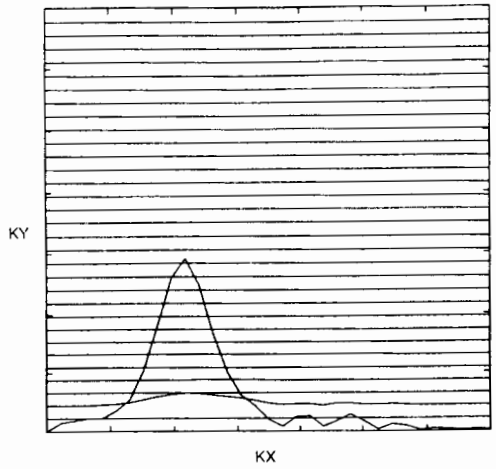

Fig. 6f

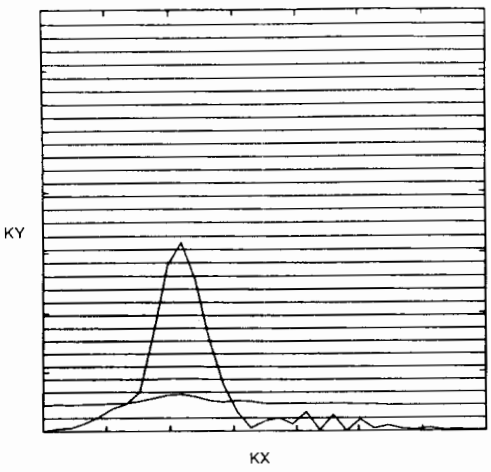

Fig. 6g

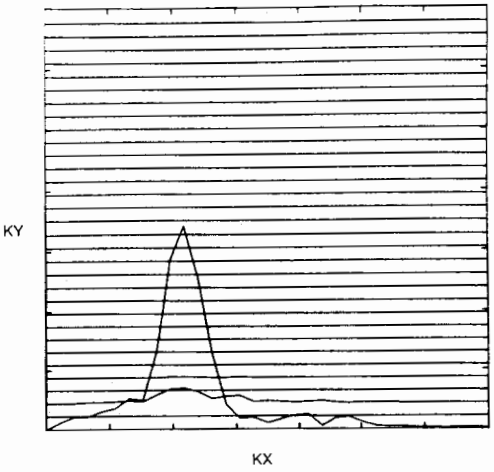

Fig. 6h

Fig. 6. (continued)

ing a fully nonlinear ship wake in the presence of a wind–generated field of gravity waves.

We have determined the effects on a single wave of a two–dimensional isotropic Phillips spectrum of sea waves. The vertical displacement of the ocean surface is given by the superposition of waves

$$h = \sum_{k_x}\sum_{k_y} a_{\mathbf{k}} \sin\left[k_x x + k_y y + 2\pi R\,(k_x, k_y)\right] \quad (47)$$

with mode amplitudes given by

$$a_{\mathbf{k}}^2 = \frac{C_0}{k^4}\,\Delta k_x\,\Delta k_y \exp\left(-k_w^2/k^2\right) \quad (48)$$

and the maximum wave number, given in terms of the average wind speed W, is $k_w = g/W^2$. The phase between wind–generated water waves is assumed to be random, so that $R\,(k_x, k_y) =$ random number from 0 to 1 for each $k_x\,k_y$ pair. The surface potential is given by a similar expression. To scale the problem to the dimensionless units of the calculation, a scale length of 100 m and wind velocity of 12 m/s were assumed. The Phillips constant C_0 was taken to be 0.030. The single pattern wave assumed had mode number 25, corresponding to a 4–m wavelength, and slope 0.020. The pattern wave decays by about a factor of 2 in amplitude in a time scale of four units, giving a decay time of $\omega_k\, t_{\text{decay}} = 60$, in approximate agreement with *Watson's* [1986] result of a decay time of about 20 s for a 4–m wavelength and a 12–m/s wind velocity, or $\omega_k\, t_{\text{decay}} = 79$. The energy is transferred, however, into waves close to the pattern wave.

3.4. *Ship Wakes*

The structure of ship waves and their interaction with an ambient wave spectrum have been studied, using 128 × 128 and 256 × 256 meshes. A surface disturbance which approximates the effect of a ship is introduced by incrementing the consecutive displacement of several spatial zones for one or more time steps, with the front of the disturbance stepped in the x coordinate in time. From the 128 × 128 mesh, the pattern was 1 × 4 spatial zones, propagating along its axis one Δx zone per time step, with the displacement increment $\Delta h = h_0/4$, $h_0 = 0.04$. For the 256 ×

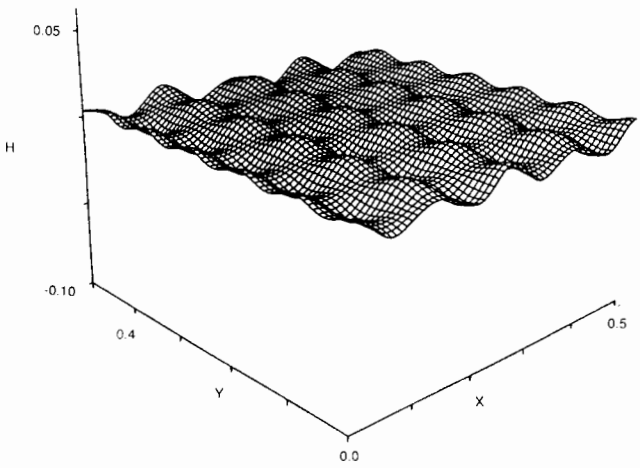

Fig. 7*a*

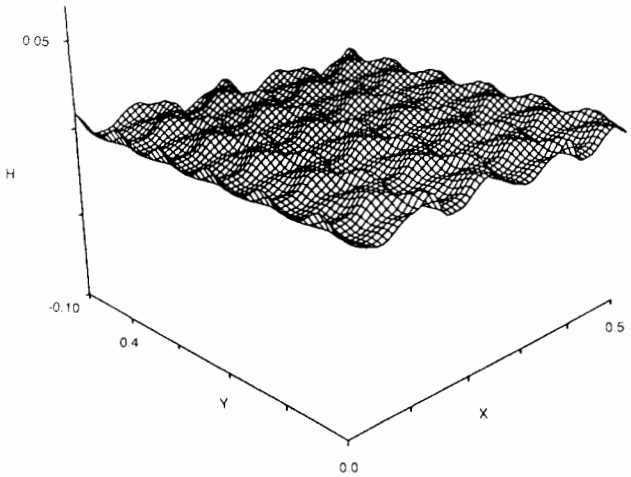

Fig. 7*b*

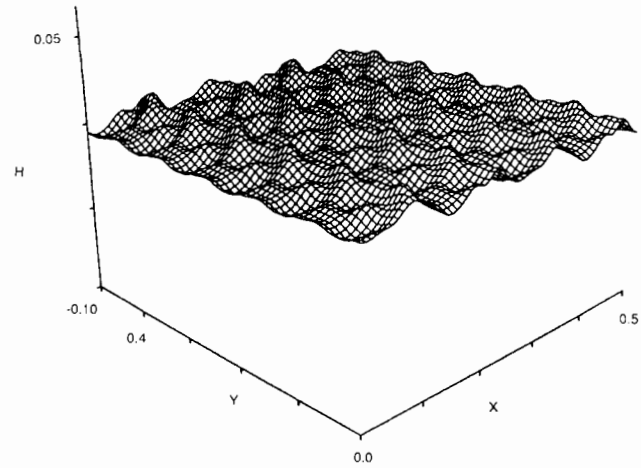

Fig. 7*c*

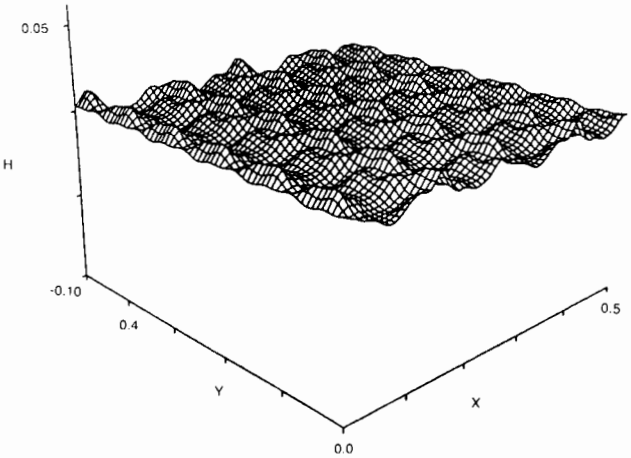

Fig. 7*d*

Fig. 7. Two-dimensional wave field showing growth of transverse cusps on a wave field. The wave amplitudes and wave numbers are given in the text. Figures 7*a*, 7*b*, 7*c*, and 7*d* are at $t = 0, 4, 8, 10$.

256 mesh, the pattern was 2×8 spatial zones, the Δt reduced by 2, and $\Delta h = h_0/8$, $h_0 = 0.04$. Since the calculational mesh is periodic, the wakes are from a "flotilla" of equally spaced ships which start to interact when the fastest waves travel from the ships to the boundary and more strongly when the strong wake reaches the boundary. As is shown in Figure 9*a*, the characteristic "Kelvin wedge" in wave amplitude is observed, together with the curving arcs predicted by *Stoker* [1957] and in *Lighthill* [1978]. Along the Kelvin wedge, a persistent marked "herringbone" pattern is also observed as shown in the contour plot in Figure 9*b*. The opening angle of the Kelvin wedge is slightly affected by the order of the calculation, becoming somewhat larger for the third-order calculation than for the linear one. The wave structure on the "herringbone" pattern was more dependent on the order, the waves being steeper and more asymmetric in the higher-order calculation.

In the presence of the background of a Phillips spectrum, the waves are rapidly dissipated, as is shown in Figure 9*c*. The effect is particularly pronounced for the 256×256 mesh with 64×64 Fourier components, showing that the waves are particularly affected by interaction with short wavelengths.

3.5. *Wave–Wave Interaction*

The Watson–West representation is formally an expansion in powers of the wave amplitude. The structure of the expansion might suggest that the convergence of the expansion may be poor if waves of very different wavelengths and amplitudes are present (see, for example, *West* [1981]). As we discussed in section 2.1 however, the series expansion is independent of the reference surface and is in fact an expansion in the surface slope at the free surface, not the reference surface. Thus we avoid the usual problem associated with the longwave–shortwave interactions, that being the convergence of the perturbation expansion for short waves with slopes of finite size. As an example, herein we have determined the time evolution of a simple one-dimensional spectrum with only two initial sinusoidal components. The surface height is given by

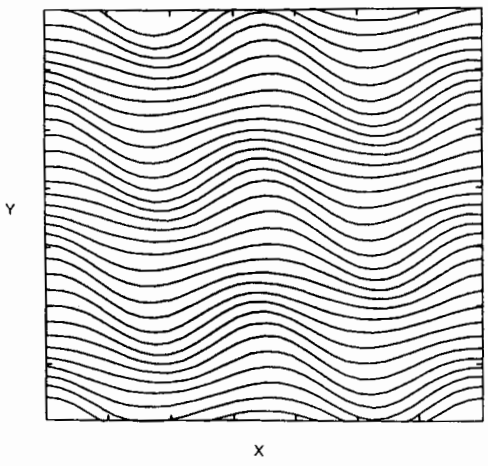

Fig. 8*a*

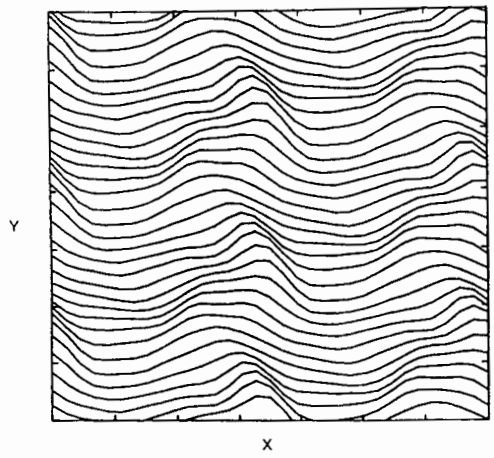

Fig. 8*b*

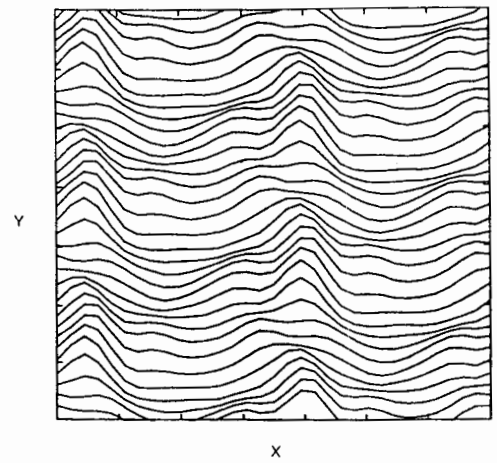

Fig. 8*c*

Fig. 8. Amplitudes of the two–dimensional wave field shown in Figure 7. The figures give 1/16 of the full wave field. The times are $t = 0, 4, 10$.

$$h = h_1 \sin k_1 x + h_2 \sin k_2 x \tag{49}$$

and the velocity potential at the surface by

$$\phi = -\frac{h_1}{\sqrt{k_1}} \cos k_1 x - \frac{h_2}{\sqrt{k_2}} \cos k_2 x \tag{50}$$

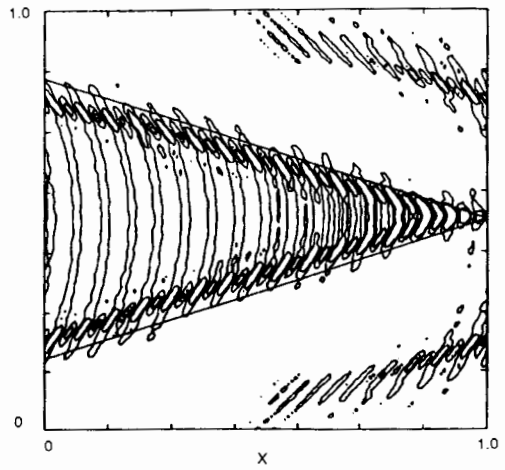

Fig. 9*a*

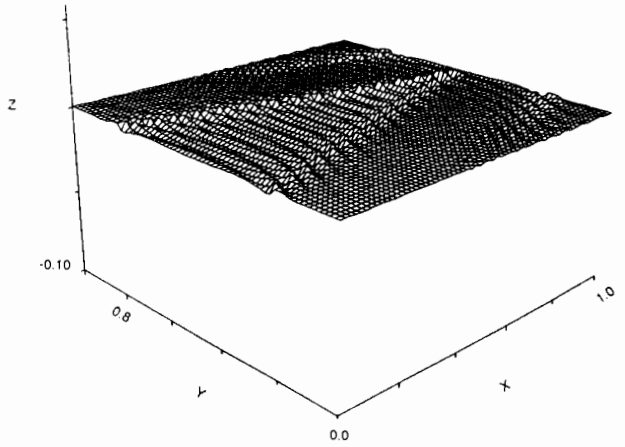

Fig. 9*b*

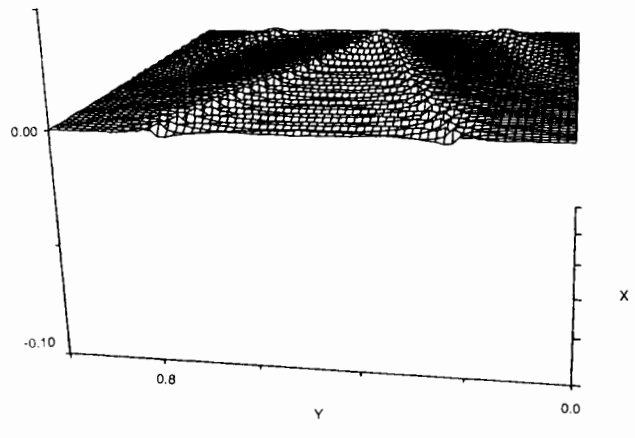

Fig. 9*c*

Fig. 9. Views of a ship wake generated by a simple linear source. Figure 9*b* gives a plan view of equal amplitude contours; the lines are at the Kelvin–wedge angle. Figures 9*a* and 9*c* are three–dimensional views of the wake from different positions.

where $k_1 = 32\pi$, $h_1 k_1 = 0.314$, $k_2 = 4\pi$, and $h_2 k_2 = 0.157$ are the wave numbers and slopes of the two spectral components. If the k_1 wave only is present, no appreciable steepening occurs. The time development of the composite

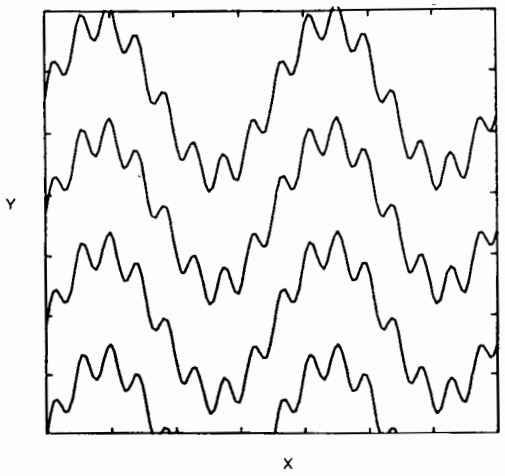

Fig. 10*a*

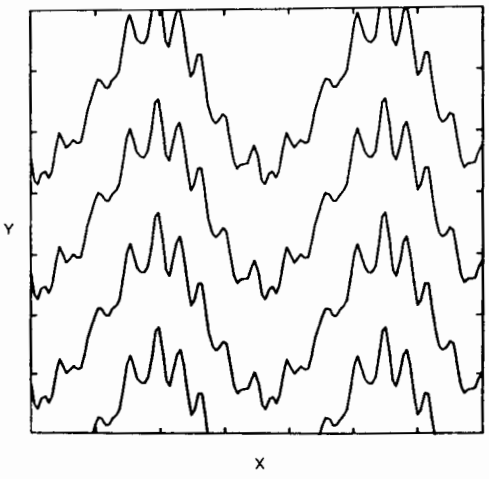

Fig. 10*b*

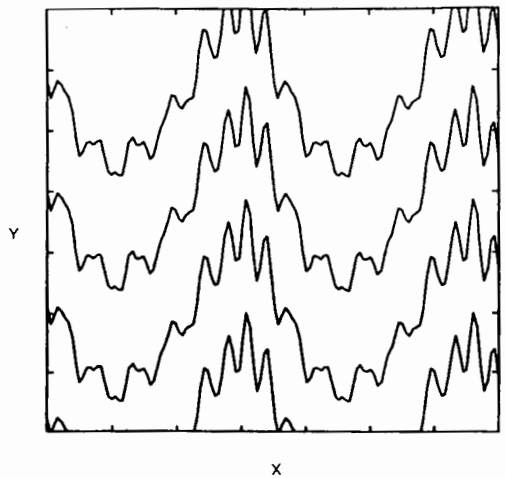

Fig. 10*c*

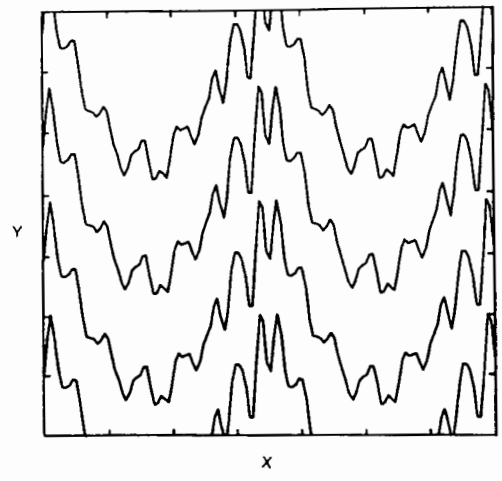

Fig. 10*d*

Fig 10. Interaction of two sinusoidal waves. The parameters are given in the text. Figures 10*a*, 10*b*, 10*c*, and 10*d*, are at $t = 0, 0.50, 1.00, 1.25$.

wave is given in Figure 10, and that of the Fourier amplitudes is given in Figure 11. In Figure 10*a* the initial superposition of the two sinusoidal water waves is given. In subsequent frames we observe the evolution of the surface on a time scale of the order of the period of the shorter wave k_1. We observe that the initially smoothly varying surface begins to suppress small oscillations in the trough of the large waves and to enhance them near the crest. After four oscillations of the small wave it is clear that the crest of the long wave is strongly distorted with most of the structure arising just behind the crest (the waves are traveling from left to right in the calculation). Close examination of the figures suggests that the location of maximum modulation of the short wave may be unsteady.

Figure 11*a* depicts the initial spectrum of the two–wave system. The evolution of the spectrum arising from nonlinear energy transfer is depicted in sequential frames corresponding to those of the surface displacement in Figure 10. These results show rapid transfer of energy into side bands of the high–frequency waves which coherently interfere to give a marked reduction in wavelength and steepening of the high–frequency wave, the effect being concentrated, near the peak of the low–frequency wave. The high–frequency, steepened waves are apparently convected with the low–frequency wave and therefore acquire a phase velocity close to that of the low–frequency wave. This strong coupling effect is consistent with the measurements of the phase speed spectral components in a laboratory wind tunnel as measured by *Ramamonjiarisoa and Coantic* [1976], in which the high–frequency waves moved at a constant phase speed near to that of the spectral peak. The present calculation indicates that the interpretation that these high–frequency waves represent a distortion of the spectral peak, rather than freely–traveling waves, may be a correct one [e.g., *Phillips*, 1978]. It is clear that the longwave–shortwave interactions are strong, so that perturbative models that obtain the equations of motion by expanding in powers of the slope of the short waves may not properly describe the shortwave modulation. The perturbative models should work while the short waves are not too steep [e.g., *Longuet–Higgins and Stewart*, 1960; *Longuet–Higgins*, 1986].

The calculation shown here is terminated after 1.25 time units. When the calculation is extended to 2.5 time units,

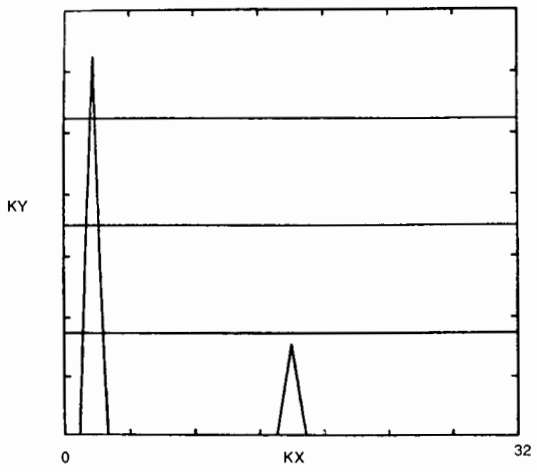

Fig. 11*a*

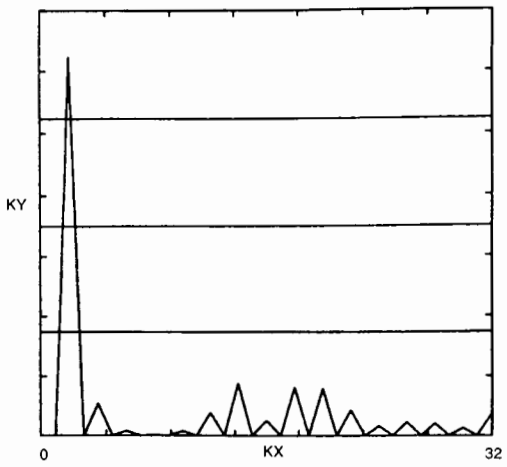

Fig. 11*b*

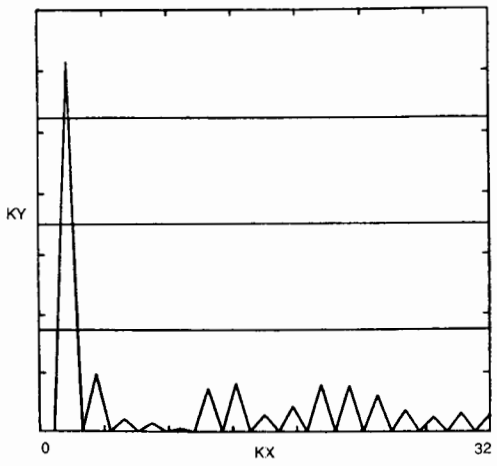

Fig. 11*c*

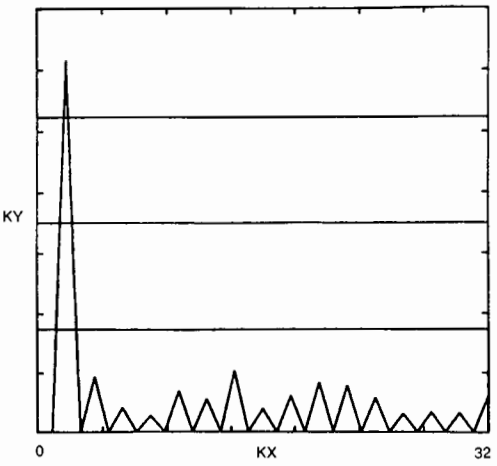

Fig. 11*d*

Fig. 11. Fourier spectra for Figure 10. The mode number is given. Figures 11*a*, 11*b*, 11*c*, and 11*d* are at $t = 0, 0.50, 1.00, 1.25$.

one observes that most of the energy contained in the high–frequency mode is returned to that mode. A low level of energy does, however, remain in the other mode contributing to the evolution. Also, the phase relation among the modes remains such that at the end of 2.5 time units the surface height resembles that in Figure 11*a* but with apparent high–frequency noise superposed. In addition, a distortion remains in advance of the crest of the low–frequency wave.

3.6. *Sharp–Crested Waves*

The following several examples illustrate the ability of this method to reproduce known nonlinear surface behavior. Perhaps the most familiar is the periodic, progressive Stokes wave. We can use either the one–dimensional or two–dimensional code to develop a nearly steady Stokes–wave counterpart for several temporal cycles by resorting to a trick, which bootstraps the simultaneous nonlinear h and ϕ fields. We multiply the nonlinear terms in the field equations by a scale factor f, which is set initially to zero, so that the dynamics are linear. The fields (h, ϕ) are initialized as a progressive steady sinusoidal solution and the factor f is then increased smoothly to unity over several cycles.

Figure 12 shows the resulting profile for a one–dimensional calculation of 128 grid points at third order in slope. The profile departs by less than 0.10% from the exact solution of the same slope.

Figure 13 compares the actual spatial overtone amplitudes to the Stokes prediction; the error bands show the residual temporal unsteadiness of the simulation. The fidelity is good out to seven harmonics even though the dynamics are nonlinear to third order. Figure 14 shows a steady Stokes–like solution generated similarly in two dimensions on a 128×128 grid.

Figure 15 illustrates the realistic coexistence of waves of dramatically different length in a single calculation. In this case the short waves are parasitic capillaries emerging from the sharp crests of a periodic gravity wave. They are added to the dynamics by means of a potential energy term

$$\int \tau[1 + (\nabla h)^2]^{1/2} \, d\mathbf{x} \tag{51}$$

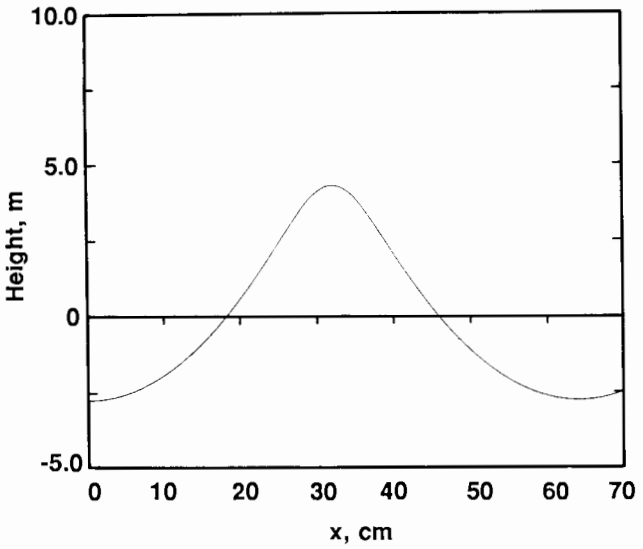

Fig. 12. This almost steady wave profile, generated by the "adiabatic bootstrap" with third–order dynamics on a grid of 128 points, differs from the exact Stokes solution by 0.10% rms. The ratio of height to wavelength is 0.110.

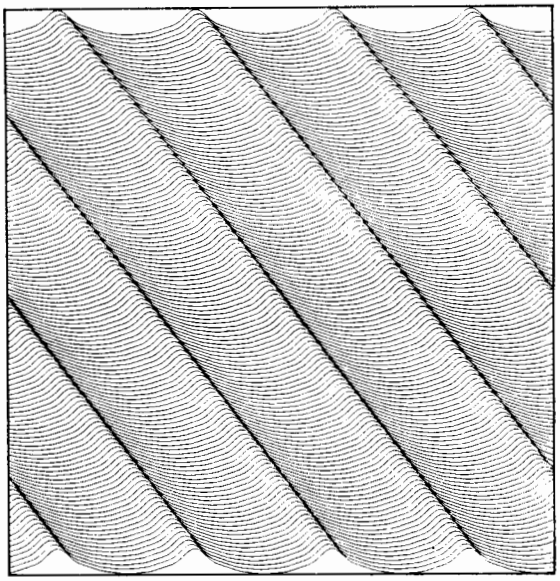

Fig. 14. An oblique periodic "Stokes" solution on a grid of 128 × 128 cells. The wave is noticeably sharp–crested at a maximum slope of 0.376.

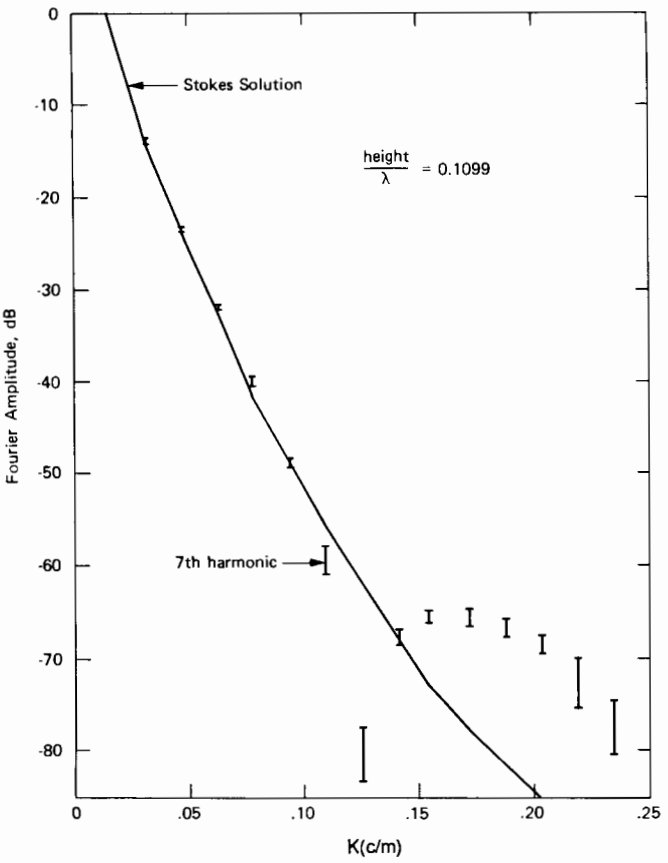

Fig. 13. The overtone spectrum of the wave in the previous figure agrees well with the Stokes values through the sixth harmonic, even with third–order dynamics. The vertical bands depict the residual temporal unsteadiness of the bootstrapped solution.

in the Hamiltonian (τ is the capillary constant) and a corresponding pressure term

$$-\tau\nabla\cdot\left\{\nabla h/\left[1+(\nabla h)^2\right]^{1/2}\right\} \tag{52}$$

in the equation (6) for $\partial\phi/\partial t$. These are exact and there is no reason to approximate them at finite order. The grid is 256 points and the solution is generated by the "adiabatic bootstrapping" described above.

The random surface shown in Figure 16 is part of a third–order dynamical simulation on a 512 × 256 grid. Meant to be ocean–like, it is based on a directionally broad

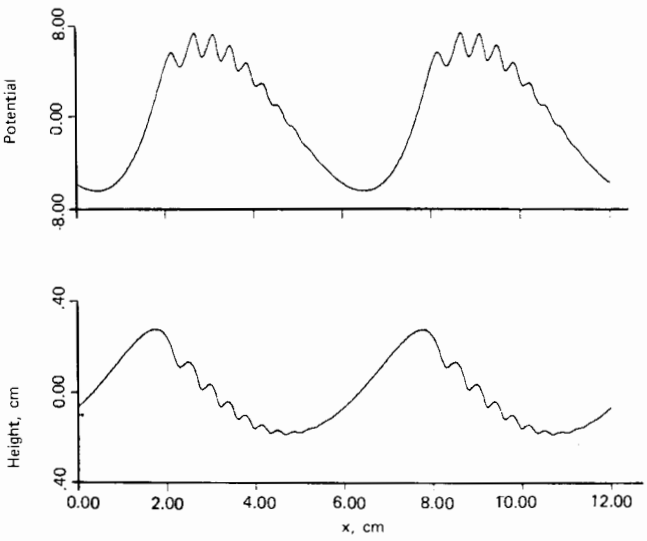

Fig. 15. A gravity wave of 6 cm wavelength has developed parasitic capillaries of 0.5 cm wavelength in this 256 point simulation. The kinetic energy is truncated to third dynamical order but the capillary force is exact. The lower curve depicts surface height and the upper depicts surface potential.

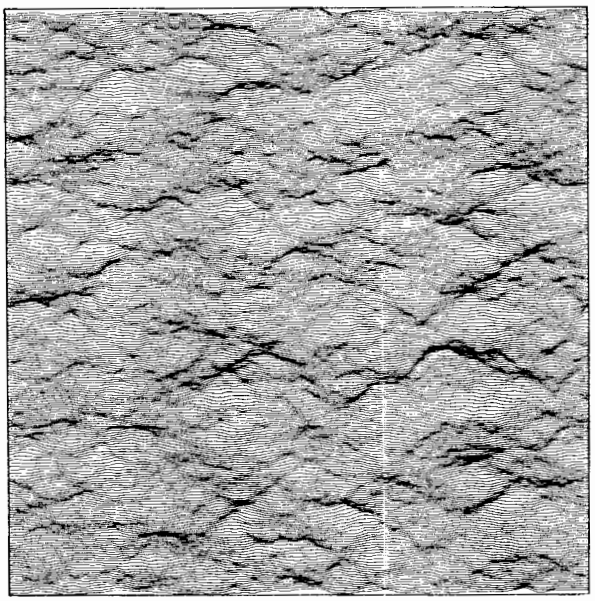

Fig. 16. This realistic looking surface resulted from a third–order dynamical simulation of random waves on a 256 × 512 grid. The corresponding height spectrum is of the form k^{-4} on a sector of angular width 120° centered in the positive vertical direction.

(120°) k^{-4} spectrum with an rms slope of 0.113. The nonlinear sharpening of the random crests is real, as the reader can verify by turning the figure upside down. A dynamically linear surface would not show such asymmetry. The maximum slope at the instant depicted is 0.649, almost six times the rms value.

4. CONCLUSIONS

We have presented an efficient numerical technique for integrating the dynamic equations for the free surface displacement of water and the velocity potential on that surface based on the formalism developed by *Watson and West* [1975]. The procedure uses a formal height expansion about the free surface of Bernoulli's equation and the kinematic boundary condition rather than an expansion about $z = 0$ that is usually done. The expansion is independent of the reference surface and is actually an expansion of the surface slope on the water surface. The integration is done by evaluating products of field quantities such as the surface displacements, surface velocities, surface gradients, etc. in configuration space; fast Fourier transforming these products and time incrementing the transformed equations to obtain the components of the appropriate field variables; then transforming (FFT) back to configuration space to again evaluate the nonlinear products and start the process again. This technique reduces the number of operations from N^2 to $N \ln N$ for an N–mode representation of the surface wave field.

In the main, those calculations involving solitons reproduced earlier results including the formation of oblique solitons (section 3.1). Of greater interest was the formation of the three–dimensional instabilities resulting from the bifurcation of three–dimensional waves arising from skew rather than colinear perturbations (section 3.2). The size, shape, and location of these instabilities were shown to agree qualitatively with experiment and analytic estimates. The calculations of the persistence of surface patterns in a wind–generated surface wave spectrum were found to be consistent with those recently obtained by others (section 3.3). There were also no surprises on the formation of the ship wakes using simple point source–generating mechanisms (section 3.4.). The longwave–shortwave interaction, when the slope of each is large, produces a strong modulation of the short waves that appears to be nearly phase–locked to the long wave. This may account for the observation that the phase speed spectral components move at a constant speed that is nearly equal to that of the spectral peak (section 3.5). This would be consistent with some earlier interpretations that the constancy in the phase speed is a consequence of the high–frequency waves not being free waves.

APPENDIX: VORTEX SHEET METHOD

A 1. *Formulation*

The vortex sheet method was developed and applied to different problems by several groups [*Longuet–Higgins*, 1976; *Pullin*, 1982; *New et al.*, 1985; *Baker et al.*, 1982], with the applications limited to two–dimensional surfaces (one horizontal and one vertical dimension). The derivation we give is similar in principle to other results but generalized to three–dimensional surfaces.

We consider a three–dimensional surface with density ρ_1 below and zero density and pressure above. The momentum equation is

$$\rho_1 \frac{d\,\mathbf{u}_1}{dt} = -\nabla p - \rho_1 \mathbf{g} \tag{A1}$$

The pressure has no transverse gradient; (A1) therefore gives

$$\hat{\mathbf{n}} \times \frac{d\,\mathbf{u}_1}{dt} = -\hat{\mathbf{n}} \times \mathbf{g} \tag{A2}$$

with $\hat{\mathbf{n}}$ the unit surface normal. The vorticity is localized to the surface across which the velocity changes from $\mathbf{u}_1$ to $\mathbf{u}_2$. The vortex sheet strength is

$$\boldsymbol{\gamma} = \hat{\mathbf{n}} \times (\mathbf{u}_2 - \mathbf{u}_1) \tag{A3}$$

The normal components of $\mathbf{u}$ are equal, i.e.,

$$\hat{\mathbf{n}} \cdot (\mathbf{u}_2 - \mathbf{u}_1) = 0 \tag{A4}$$

We define the average velocity at the interface as

$$\mathbf{q} = \frac{1}{2}(\mathbf{u}_1 + \mathbf{u}_2) \tag{A5}$$

so that (A3), (A4), and (A5) give

$$\mathbf{u}_1 = \mathbf{q} + \frac{1}{2}\hat{\mathbf{n}} \times \boldsymbol{\gamma} \tag{A6}$$

Equation (A2) therefore gives

$$\hat{\mathbf{n}} \times \frac{d}{dt}(\hat{\mathbf{n}} \times \boldsymbol{\gamma}) = -2\hat{\mathbf{n}} \times \left[\mathbf{g} + \frac{d\mathbf{q}}{dt}\right] \tag{A7}$$

In (A1)–(A6), the convective time derivative is

$$\frac{d}{dt} = \frac{\partial}{\partial t} + \mathbf{u}_1 \cdot \nabla$$

The left side of (6) can be rewritten as

$$\hat{\mathbf{n}} \times \left[\left(\frac{d\hat{\mathbf{n}}}{dt} \right) \times \boldsymbol{\gamma} \right] + \hat{\mathbf{n}} \times \left[\hat{\mathbf{n}} \times \frac{d\boldsymbol{\gamma}}{dt} \right] =$$

$$\frac{d\hat{\mathbf{n}}}{dt} \hat{\mathbf{n}} \cdot \boldsymbol{\gamma} - \hat{\mathbf{n}} \cdot \frac{d\hat{\mathbf{n}}}{dt} \boldsymbol{\gamma} + \hat{\mathbf{n}}\hat{\mathbf{n}} \cdot \frac{d\boldsymbol{\gamma}}{dt} - \frac{d\boldsymbol{\gamma}}{dt} \qquad \text{(A8)}$$

In this equation, $\hat{\mathbf{n}} \cdot \boldsymbol{\gamma} = 0$, $(d/dt)(\hat{\mathbf{n}} \cdot \hat{\mathbf{n}}) = \hat{\mathbf{n}} \cdot (d\hat{\mathbf{n}}/dt) = 0$, $(d/dt)(\hat{\mathbf{n}} \cdot \boldsymbol{\gamma}) = (d\hat{\mathbf{n}}/dt) \cdot \boldsymbol{\gamma} + \hat{\mathbf{n}} \cdot (d\boldsymbol{\gamma}/dt) = 0$. Equations (A6) and (A7) therefore combine to give

$$\frac{d\boldsymbol{\gamma}}{dt} + \boldsymbol{\gamma} \cdot \frac{d\hat{\mathbf{n}}}{dt} = 2\hat{\mathbf{n}} \times \left(\mathbf{g} + \frac{d\mathbf{q}}{dt} \right) \qquad \text{(A9)}$$

Equation (A9) gives the time evolution of the sheet vorticity with the convective derivatives following the motion of the dense fluid. For the two–dimensional problem $(x - z)$ the vorticity is in the y direction, the surface normal $\hat{\mathbf{n}}$ in the x, y plane, and the second term in (A9) is zero.

The velocity $\mathbf{u}_1$ must be determined from $\boldsymbol{\gamma}$. The vorticity in either fluid is

$$\boldsymbol{\omega} = \nabla \times \mathbf{u} \qquad \text{(A10)}$$

We define a stream function by

$$\mathbf{u} = \nabla \times \boldsymbol{\psi} \qquad \text{(A11)}$$

giving

$$\nabla^2 \boldsymbol{\psi} - \nabla \operatorname{div} \boldsymbol{\psi} = -\boldsymbol{\omega} \qquad \text{(A12)}$$

A gauge can always be chosen for which $\boldsymbol{\psi} = 0$. Equation (A12) has the formal solution

$$\boldsymbol{\psi}(\mathbf{r}) = -\int G(\mathbf{r} - \mathbf{r}') \boldsymbol{\omega}(\mathbf{r}') d^3 r' \qquad \text{(A13)}$$

The integral of the vorticity across the surface is $\boldsymbol{\gamma}$. Equation (A13) therefore can be rewritten

$$\boldsymbol{\psi}(\mathbf{r}) = -\int G(\mathbf{r} - \mathbf{r}') \boldsymbol{\gamma} d^2 s' \qquad \text{(A14)}$$

with $d^2 s'$ the element of surface area along the interface. The Green's function for a system without periodic boundary conditions is

$$G(\mathbf{r}) = \frac{1}{4\pi |\mathbf{r}|} \qquad \text{(A15)}$$

In (A13) the principal part of the integral is to be taken. Correspondingly, the velocities from (A11) are the averages across the vortex sheet. From the vortex sheet strength and $\mathbf{q}$, the fluid velocity $\mathbf{u}_1$ necessary to determine the motion of the vortex element is obtained from (A6).

For periodic boundary conditions, the Green's function can be obtained by summing $G(\mathbf{r})$ over a lattice in coordinate space or by restricting the horizontal wave number sums in Fourier space. This is computationally tedious in two surface dimensions but straightforward on a regular grid from which the spatially varying function can be obtained by interpolation.

2. *Vortex Sheet Computations*

The principal computational difficulty is the evaluation of the coupled equations for $\boldsymbol{\gamma}$ and $\mathbf{u}$. Since $\mathbf{u}$ is coupled to $\boldsymbol{\gamma}$ by a matrix $G(\mathbf{r} - \mathbf{r}')$, a straightforward procedure used by Longuet–Higgins and Pullin is the inversion at each time step of the matrix equation coupling $\mathbf{u}$ to $\boldsymbol{\gamma}$. This is possible, although nontrivial in the two–dimensional problem but a major computing requirement for the two–dimensional problem with 10^4 to 10^6 surface elements. The matrix inversion was avoided by *Baker et al.* [1982], who solved the coupled equations by multiple iteration. This again is relatively simple in two–dimensions but difficult in three–dimensions. The three–dimensional problem is also increased in difficulty by the necessity of determining the three–dimensional stream function $\boldsymbol{\psi}$, while the two–dimensional calculation needs the scalar function ψ_y. These problems can be reduced by use of FFTs. This requires, however, Fourier expansion of the Green's function, and power series expansion of the exponential factor $\exp[-|\mathbf{k}| z(x, y)]$. If this is done, the three–dimensional calculation still requires evaluation of the three dimensional stream function. It should be noted that the slope expansion, necessary for use of FFT, also prevents the vortex sheet method from being used for study of very steep or breaking waves, which have been successfully computed only in two dimensions.

For the above reasons, the vortex sheet method has not (to our knowledge) been used in three dimensions. The procedure given in section 2 is relatively straightforward, avoids some of the problems of the vortex sheet method, and is computationally much more efficient.

Acknowledgments. This work was supported in part by the La Jolla Institute Independent Research and Development Funds, the San Diego Supercomputer Center, and the DARPA/URI grant number N00014-86-K-0758.

REFERENCES

Baker, G. R., D. I. Meiron, and S. A. Orszag, Generalized vortex methods for free–surface flow problems, *J. Fluid Mech., 123*, 477–501, 1982.

Benjamin, T. B., and J. E. Feir, The disintegration of wave trains on deep water, I, Theory, *J. Fluid Mech. 27*, 417–430, 1967.

Benney, D. J., Nonlinear gravity wave interactions, *J. Fluid Mech., 14*, 577–589, 1962.

Broer, L. J. F., On the Hamiltonian theory of surface waves, *Appl. Sci. Res., 30*, 430–466, 1974.

Bryant, P. J., Nonlinear wave groups in deep water, *Stud. Appl. Math., 61*, 1–30, 1979.

Bryant, P. J., Oblique wave groups in deep water, *J. Fluid Mech., 146*, 1–20, 1984.

Chirkov, B., A universal instability of many–dimensional oscillator systems, *Phys. Rep., 52*, 263–379, 1979.

Cohen, B. I., K. M. Watson, and B. J. West, Some properties of deep water solitons, *Phys. Fluids, 19*, 345–354, 1976.

Dungey, J. C. and W. H. Hui, Nonlinear energy transfer in a narrow gravity–wave spectrum, *Proc. R. Soc. London, Ser A, 368*, 239–265, 1979.

Fox, M. J. H., On the nonlinear transfer of energy in the peak of a gravity wave spectrum. II, *Proc. R. Soc. London Ser. A, 348*, 467, 1976.

Hasselmann, K., On the nonlinear energy transfer in a gravity–wave spectrum, I, General theory, *J. Fluid Mech., 12*, 481–500, 1962, *15*, II, Conservation theorems, wave–particle correspondence, irreversibility, 237–281, 1963*a*, III, Evaluation of the energy flux and swell-sea interaction for a Neumann spectrum, *15*, 385, 1963*b*.

Hasselmann, K., Weak–interaction theory of ocean waves, in

Basic Development in Fluid Mechanics, vol. 2, edited by M. Hoyt, pp. 117–182, Academic, Orlando, Fla., 1968.

Hasselmann, S., and K. Hasselmann, A symmetric method of computing the nonlinear transfer in a growth–wave spectrum, *Hamb. Geophys. Einzelschr., Reihe A, Wiss. Abh., 52*, 1–138, 1981.

Hasselmann, S., and K. Hasselmann, Computation and parameterization of the nonlinear energy transfer in a gravity–wave spectrum, I, A new method for efficient calculations of the exact nonlinear transfer integral, *J. Phys. Oceanogr. 15*, 1369–1377, 1985.

Herterich, K., and K. Hasselmann, A similarity relation for the nonlinear energy transfer in a finite depth gravity–wave spectrum, *J. Fluid Mech., 97*, 215–244, 1980.

Hui, W. H., and J. Hamilton, Exact solutions of a three–dimensional nonlinear Schrödinger equation applied to gravity waves, *J. Fluid Mech., 93*, 117–133, 1979.

Lake, B. M., H. C. Yuen, H. Rungaldier, and W. E. Ferguson, Nonlinear deep water waves: Theory and experiment, II, Evolution of a continuous wave train, *J. Fluid Mech., 83*, 49–74, 1977.

Lighthill, J., *Waves in Fluids*, Cambridge University Press, New York, 1978.

Longuet–Higgins, M. S., Resonant interactions between two trains of gravity waves, *J. Fluid Mech., 12*, 321, 1962.

Longuet–Higgins, M. S., On the nonlinear transfer of energy in the peak of a gravity wave spectrum: a simplified model, *Proc. R. Soc. London, Ser. A, 347*, 311–328, 1976.

Longuet–Higgins, M. S., and E. D. Cokelet, The deformation of steep surface waves on water I, a numerical method of computation, *Proc. R. Soc. London, Ser. A, 350*, 1, 1976.

Longuet–Higgins, M. S., The propagation of short surface waves on longer gravity waves, *J. Fluid Mech., 177*, 293–306, 1987.

Longuet–Higgins, M. S., and R. W. Stewart, Changes in the form of short gravity waves on long waves and tidal currents, *J. Fluid Mech., 8*, 565–583, 1960.

Martin, D. U., P. G. Saffman, and H. C. Yuen, Stability of plane wave solutions of the two–space–dimensional nonlinear Schrödinger equation, *Wave Motion, 2*, 215–229, 1980.

McLean, J. W., Instabilities of finite–amplitude water waves, *J. Fluid Mech., 114*, 315–330, 1982.

McLean, J. W., Y. C. Ma, D. V. Martin, P. G. Saffman, and H. C. Yuen, Three–dimensional instability of finite amplitude water wave, *Phys. Rev. Lett., 46*, 817–820, 1981.

Milder, M., A note regarding 'On Hamilton's principle for surface waves,' *J. Fluid Mech., 83*, 159–161, 1977.

Miles, J. W., On Hamilton's principle for surface waves, *J. Fluid Mech., 83*, 153–164, 1977.

Moser, J., *Stable and Random Motions in Dynamical Systems*, Princeton University Press, Princeton, NJ, 1973.

New, A. L., P. McIver, and D. H. Peregrine, Computations of overturning waves, *J. Fluid Mech., 150*, 233, 1985.

Peregrine, D. H., Water waves, nonlinear Schrödinger equations and their solutions, *J. Aust. Math. Soc., B24*, 16–43, 1983.

Peregrine, D. H., and G. P. Thomas, Finite amplitude deep–water waves on currents, *Proc. R. Soc. London, Ser. 292*, 371–389, 1979.

Phillips, O. M., On the dynamics of unsteady gravity of finite amplitude, *J. Fluid Mech. 9*, 193–217, 1960.

Phillips, O. M., *The Dynamics of the Upper Ocean*, Cambridge University Press, New York, 1966.

Phillips, O. M., Strong interactions in wind–wave fields, in *Turbulent Fluxes Through the Sea Surface, Wave Dynamics and Predictions*, edited by A. Favre and K. Hasselmann, pp. 373–384, Plenum, New York, 1978.

Pullin, D. I., Numerical studies of surface–tension effects in nonlinear Kelvin–Helmholtz and Rayleigh–Taylor instability, *J. Fluid Mech., 119*, 507–532, 1982.

Ramamonjiarisoa, A. and M. Coantic, Loi expérimentale de dispersion de vagues produits par le vent sur sine faible longueur d'action, *C. R. Acad. Sci. Paris, Ser. B, 282*, 111–113, 1976.

Saffman, P. G., and H. C. Yuen, Stability of a plane solution to infinitesimal two–dimensional perturbations, *Phys. Fluids, 21*, 1450–1451, 1978.

Saffman, P. G., and H. C. Yuen, A new type of three–dimensional deep–water wave of permanent form, *J. Fluid Mech., 101*, 797–808, 1980.

Stoker, J. J., *Water Waves*, Interscience, New York, 1957.

Su, M. Y., Three–dimensional deep–water waves, I, Experimental measurement of skew and symmetric wave patterns, *J. Fluid Mech., 124*, 73–108, 1982.

Su, M. Y., and A. W. Green, On predictability of deep–water waves, *AIP Conf. Proc. 106*, 507–514, 1984.

Su, M. Y., M. Bergin, P. Morler, and R. Myrick, Experiments on nonlinear instabilities and evolution of steep gravity–wave trains, *J. Fluid Mech., 124*, 45–72, 1982.

Watson, K. M., Persistence of a pattern of surface gravity waves, *J. Geophy. Res., 91*, 2607–2622, 1986.

Watson, K. M., and B. J. West, A transport–equation description of nonlinear ocean surface wave interactions, *J. Fluid Mech 70*, 815–826, 1975.

Watson, K. M., B. J. West, and B. I. Cohen, Coupling of surface and internal gravity waves: a mode coupling model, *J. Fluid Mech., 77*, 185–208, 1976.

West, B. J., *Deep Water Gravity Waves*, Springer, New York, 1981.

Yuen, H. C., and B. M. Lake, Nonlinear dynamics of deep–water gravity waves, in *Advances in Applied Mechanics*, vol. 22, pp. 67–229, Academic, Orlando, Fla., 1982.

Zakharov, V. E., Stability of periodic waves of finite amplitude on the surface of a deep fluid, *J. Appl. Mech. Tech. Phys.*, Engl. Transl., 2, 190–194, 1968.

Zakharov, V. E. and A. B. Shabat, Exact theory of two–dimensional self–focusing and one–dimensional self–modulating waves in nonlinear media, *Sov. Phys. JETP*, Engl. Transl., *65*, 997–1011, 1972.

(Received October 27, 1986;
accepted February 12, 1987.)